# Insights into the Chemomechanical Coupling of the Myosin Motor from Simulation of Its ATP Hydrolysis Mechanism†

Sonja M. Schwarzl,‡,§ Jeremy C. Smith,§ and Stefan Fischer*,‡

*Computational Biochemistry, Interdisciplinary Center for Scientific Computation, University of Heidelberg, Im Neuenheimer Feld 368, 69120 Heidelberg, Germany, and Computational Molecular Biophysics, Interdisciplinary Center for Scientific Computation, University of Heidelberg, Im Neuenheimer Feld 368, 69120 Heidelberg, Germany*

*Received November 29, 2005; Revised Manuscript Received March 14, 2006*

ABSTRACT: The molecular motor myosin converts chemical energy from ATP hydrolysis into mechanical work, thus driving a variety of essential motility processes. Although myosin function has been studied extensively, the catalytic mechanism of ATP hydrolysis and its chemomechanical coupling to the motor cycle are not completely understood. Here, the catalysis mechanism in myosin II is examined using quantum mechanical/molecular mechanical reaction path calculations. The resulting reaction pathways, found in the catalytically competent closed/closed conformation of the Switch-1/Switch-2 loops of myosin, are all associative with a pentavalent bipyramidal oxyphosphorane transition state but can vary in the activation mechanism of the attacking water molecule and in the way the hydrogens are transferred between the heavy atoms. The coordination bond between the $Mg^{2+}$ metal cofactor and Ser237 in the Switch-1 loop is broken in the product state, thereby facilitating the opening of the Switch-1 loop after hydrolysis is completed, which is required for subsequent strong rebinding to actin. This reveals a key element of the chemomechanical coupling that underlies the motor cycle, namely, the modulation of actin unbinding or binding in response to the ATP or ADP·$P_i$ state of nucleotide-bound myosin.

Molecular motors utilize energy from nucleoside triphosphate hydrolysis to enable cells to move, contract, secrete, endocytose, and organize their cytoplasm (*1*). All members of the myosin superfamily of motors (*2*, *3*) hydrolyze ATP and interact cyclically with actin, moving along actin filaments. Because the nucleotide binding pocket of myosins is similar to the active site of kinesins (*4*), $F_1$-ATPase, and GTPases (*5*, *6*), it has been suggested that these enzymes use similar strategies to catalyze hydrolysis and may have evolved from a common ancestor (*7*).

The molecular mechanism of myosin (reviewed in refs *8*−*10*) has been studied extensively. Myosin II is composed of a heavy chain and two light chains. The N-terminal globular domain of the heavy chain contains both the catalytic site and the actin-binding region. It has been shown that the N-terminal domain alone is able to hydrolyze ATP and to move along an actin filament (*11*). The detailed mechanism of the ATP hydrolysis is still unclear, yet this step is essential since it triggers the increase in the affinity of nucleotide-bound myosin for actin, thus permitting the binding of myosin to actin before the power stroke. In this study, we use computational methods to examine the hydrolysis mechanism and analyze how the reaction might be coupled to the structural elements controlling actin binding.

† S.M.S. was supported by the Boehringer Ingelheim Fonds and the Deutsche Forschungsgemeinschaft (DFG).

* To whom correspondence should be addressed. E-mail: stefan.fischer@iwr.uni-heidelberg.de. Phone: +49-6221-54-8879. Fax: +49-6221-54-8868.

‡ Computational Biochemistry.

§ Computational Molecular Biophysics.

The hydrolytic activity of myosin in the absence of actin follows an enzymatic cycle depicted in Figure 1A, which is based on extensive kinetic characterization of *Dictyostelium discoideum* myosin II (termed "myosin" hereafter). After ATP binds to myosin, the protein changes its conformation from the post-power-stroke to the prehydrolysis conformation. A pathway through configurational space for this conformational change has recently been described (*12*). Hydrolysis is followed by phosphate release and, subsequently, ADP release. Both product release events are coupled to conformational changes, as myosin changes its structure from the posthydrolysis conformation via the pre-power-stroke structure to the post-power-stroke conformation.

Assuming the standard Eyring rate law, the kinetics of Figure 1A can be represented in a free energy diagram, shown in Figure 1B. This work is concerned with only the ATP hydrolysis step, 3b. Although the reaction free energy of the whole hydrolysis cycle under standard-state conditions is −7.4 kcal/mol (see Methods), the free energy change corresponding to the actual hydrolysis event of step 3b is only approximately −2 kcal/mol. The barrier height of the uncatalyzed hydrolysis in solution [28.9−29.3 kcal/mol (*13*, *14*)] is halved to ∼14.5 kcal/mol in the myosin-catalyzed hydrolysis in step 3b.

The ATP-binding pocket in myosin is formed by three loops: the phosphate-binding loop (P-loop), the Switch-1 loop, and the Switch-2 loop (Figure 2B). The sequences of these loops are conserved among the myosin superfamily, with the consensus sequences GESGAGKT (P-loop), Nx-NSSR (Switch-1), and DxSGFE (Switch-2) (*15*). Both

10.1021/bi052433q CCC: $33.50 
Published on Web 04/15/2006

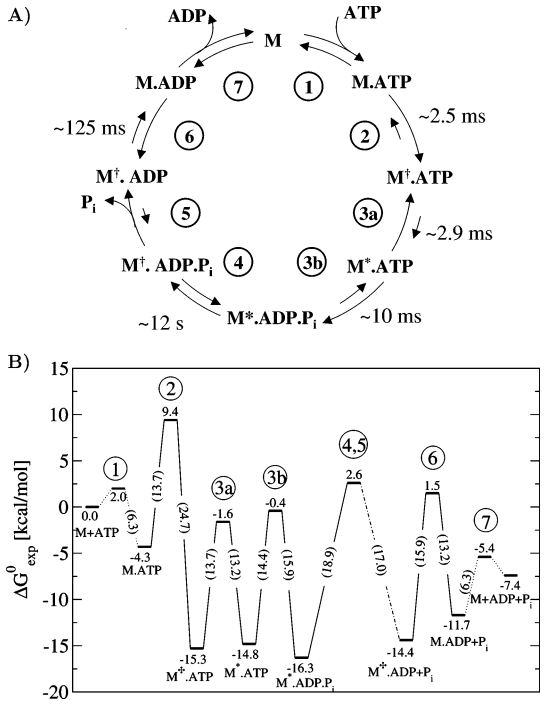


FIGURE 1: Kinetic cycle for ATP hydrolysis by *D. discoideum* myosin II in the absence of actin as derived from kinetic fits to fluorescence measurements using a protein construct termed W501+ that contained only one fluorescent tryptophan, W501 (*39*). (A) In step 1, ATP binds to apomyosin (M), thus forming a collision complex (M·ATP), presumably with both Switch-1 and Switch-2 loops open (O/O state). This is followed by a conformational change of myosin as monitored by a quench in the fluorescence intensity (step 2), leading to M*·ATP that presumably corresponds to the closing of Switch-1 (C/O state). In step 3a, fluorescence enhancement is observed, leading to M*·ATP, presumably corresponding to closing of Switch-2 (C/C state), coupled with the recovery stroke of the lever arm. The catalysis of ATP hydrolysis (step 3b) takes place exclusively when myosin is in its C/C conformation. Hydrolysis is followed by a conformational change indicated by a quench in fluorescence (step 4, $M^{\dagger}\cdot ADP\cdot P_i$, presumably the start of the power stroke) and subsequent phosphate release (step 5, $M^{\dagger}\cdot ADP$). Another conformational change occurs, restoring the fluorescence intensity of the apo structure (step 6, M·ADP) that precedes ADP release (step 7). The time constants [i.e., the reciprocal of the measured rate constants (*37*, *39*, *43*)] for forward reaction steps are given. (B) Corresponding free energy profile under standard conditions (293 K, all species at a concentration of 1 M) constructed from experimental measurements (see Methods). Under physiological concentrations (differing from the 1 M standard state), under steady-state conditions, and in the presence of actin, the free energy profile of the contraction cycle is significantly different (*38*).

Switch-1 and Switch-2 can assume either an open or a closed conformation. Only the Switch-1 closed/Switch-2 closed (C/C) conformation is catalytically active (*9*). A number of isotope exchange studies aiming at elucidating details of the reaction mechanism of ATP hydrolysis in myosin have been reported (reviewed in ref *16*). These have established that hydrolysis step 3b is reversible and that water can enter and leave the closed active site in the C/C conformation (*17*, *18*). The three terminal $\gamma$-oxygens (see Figure 2A for atom nomenclature) were found to exchange equivalently with bulk water (solvent−phosphate exchange), whereas no exchange between the $\beta$-nonbridge and the $\beta\gamma$-bridge oxygens (positional oxygen isotope exchange) was observed (*19*−*21*), indicating significant rotational freedom of either the $\gamma$-phosphate moiety of ATP or the bound inorganic phosphate, $P_i$,[1] while the ADP moiety remains positionally invariant.

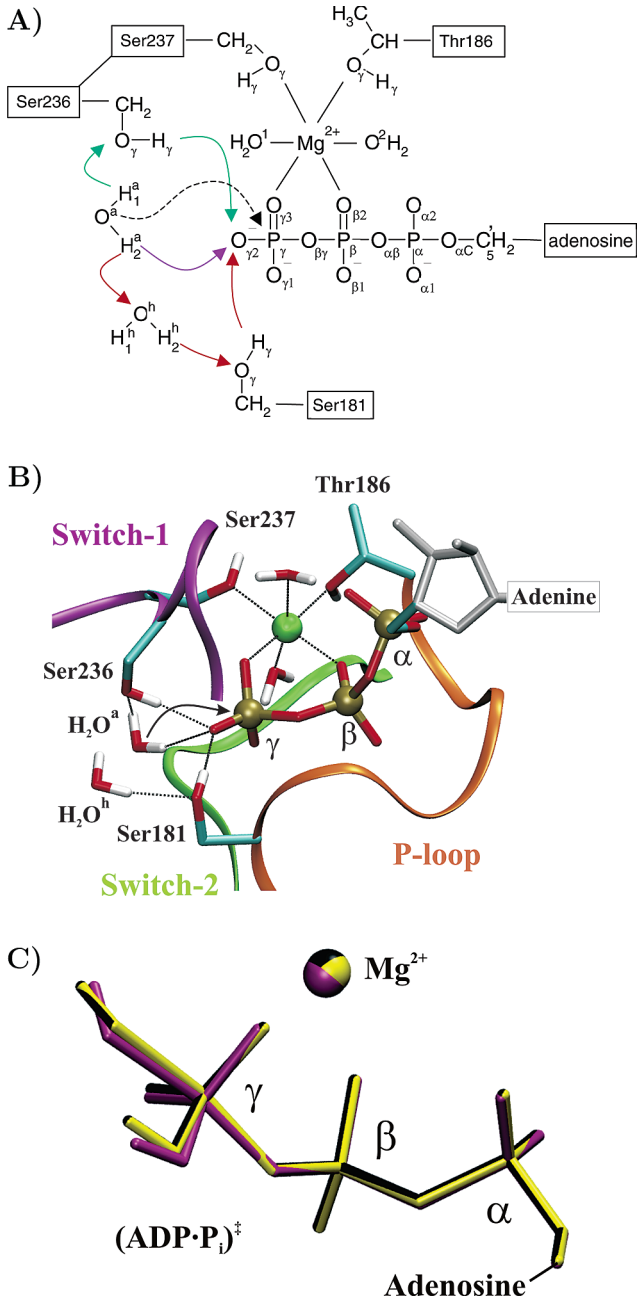


FIGURE 2: (A) Possible reaction pathways for ATP hydrolysis. Three different mechanisms of water activation are shown, each with its proton transfer steps in a different color: the violet arrow corresponds to the direct path, red arrows correspond to the Ser181 path, and green arrows correspond to the Ser236 path. The dashed arrow shows the attack of the activated water on the $\gamma$-phosphate. All the atoms treated with QM in the calculations are shown explicitly. (B) Nucleotide binding site of the reactant state, optimized with HF/6-31G(d,p). (C) Overlap of the transition-state structures of the nucleotide in the direct (black), Ser181 (purple), and Ser236 (yellow) paths optimized with HF/6-31G(d,p).

Measurements of the time course of oxygen exchange revealed that hydrolysis is likely to proceed via a single-step mechanism without a stable intermediate (*22*).

The mechanism of a phosphate hydrolysis reaction can, in principle, lie anywhere between a purely associative

[1] Abbreviations: $P_i$, inorganic phosphate; MTP, methyl triphosphate; TS, transition state; CPR, conjugate peak refinement; QM/MM, quantum mechanics/molecular mechanics; rms, root-mean-square; EPR, electron paramagnetic resonance.

mechanism, in which the attacking nucleophile enters the reaction prior to formation of a pentacovalent oxyphosphorane intermediate, and a purely dissociative mechanism, in which ATP dissociates into ADP and a metaphosphate ($PO_3^-$) intermediate in a first step and the nucleophile enters the reaction in a second step. Disruption of the myosin-catalyzed ATP hydrolysis reaction, by quenching with $HClO_4$ containing $^{18}O$-labeled water, revealed that the attacking water binds to the $\gamma$-phosphate prior to formation of the transition state (*23*), thus ruling out a phosphorylated side chain or a detectable metaphosphate intermediate. It thus seems likely that hydrolysis proceeds via an associative-like mechanism. If one terminal $\gamma$-oxygen of ATP is replaced with sulfur, the hydrolysis step becomes rate-limiting and irreversible, thus preventing isotope exchange (*24*). The use of an ATP analogue with three distinguishable atoms in the $\gamma$-nonbridge positions ([$\beta\gamma$-$^{18}O$;$\gamma$-$^{18}O_1$]ATP$\gamma$S) in $^{17}O$-labeled bulk water showed that hydrolysis proceeds with inversion of the pyramidal configuration at $P_\gamma$ (*24*), thus excluding a phosphorylated intermediate as well as a pseudorotation mechanism [a conformational change in which two axial ligands of the pentavalent trigonal bipyramid interconvert their positions with two equatorial ligands (*25*, *26*)]. Furthermore, bond-order analysis based on Raman difference spectroscopic measurements on a myosin·Mg·ADP·$VO_4$ complex suggested that the reaction has the character of a concerted $S_N2$ mechanism (*27*), again indicating that the mechanism is more associative than dissociative.

A number of associative reaction mechanisms have been proposed, differing in the way the attacking water is activated. These include (1) "direct" activation, in which the attacking water directly transfers a proton to the $\gamma$-phosphate moiety of ATP (*28*, *29*), (2) the "Ser236 mechanism", in which the side chain of Ser236[2] is involved in a proton relay (*28*, *29*), (3) the "Ser181 mechanism", analogous to mechanism 2 but involving Ser181 (*30*), (4) a mechanism in which Lys185 acts as a general base that abstracts a proton from the attacking water (*30*), (5) a mechanism in which Lys185 acts as a general acid that protonates the $\gamma$-phosphate moiety of ATP (*31*), and (6) a "two-water hypothesis", in which the attacking water is activated by a second water molecule in the active site which, in turn, is positioned by Glu459 and Gly457 (*32*). Mutational studies have shown that replacing either Ser181 (*33*) or Ser236 (*34*) with Ala does not abolish hydrolysis.

Computational methods combining a quantum mechanical/molecular mechanical (QM/MM) description of the protein have also been used to analyze the hydrolysis mechanism. In QM/MM calculations, the reactive site is modeled quantum mechanically, thus allowing processes involving bond breaking and making to be described, with effects from the protein environment included in a computationally feasible way using molecular mechanics. Previous QM/MM calculations on the ATP hydrolysis mechanism in myosin confirmed that indeed only the C/C conformation of myosin is competent for hydrolysis (*35*). These calculations suggested that hydrolysis occurs via a stable pentacovalent oxyphosphorane intermediate, in contrast to results from a purely ab initio quantum chemical study on a simplified active site model of myosin which concluded that the mechanism proceeds without a stable intermediate (*36*). Finally, a semiempirical molecular orbital study of an active site model suggested significant charge transfer between the reacting Mg·ATP species and the protein (*30*).

Although much insight has been provided by the experimental and theoretical studies cited above, a number of major questions remain open. These include the degree of associativity of the reaction mechanism and whether there is a stable intermediate. The specific role of the protein environment also remains unclear, as indicated by a lack of consensus about the activation mechanism of the attacking water. This study thus explores three of the proposed water activation mechanisms, namely, the direct, Ser236, and Ser181 mechanisms (see Figure 2A), by computing QM/MM minimum energy reaction paths. The results provide new insight into the enzymatic strategy of myosin and the early events following the hydrolysis step. It is found that hydrolysis proceeds via an associative route and an unstable pentavalent oxyphosphorane. The three water activation mechanisms are found to be equally likely within the accuracy of the available quantum methods. Of particular interest to the chemomechanical coupling in myosin, it is found that immediately after hydrolysis the connection between the Switch-1 loop and the $Mg^{2+}$ coordination sphere is broken, preparing for the subsequent opening of Switch-1 that is believed to occur upon binding of actin and is necessary for the release of the hydrolysis products during the power stroke.

## METHODS

*Experimental Free Energy Profile.* The free energy profile of the myosin cycle shown in Figure 1B was derived as follows. The reaction free energies ($\Delta_R G$) were calculated from the experimental equilibrium constants ($K$) according to $\Delta_R G = -RT \ln K$, where $R$ is the ideal gas constant and $T$ is the absolute temperature (293 K), assuming a standard concentration of 1 M for all species. The barrier heights ($\Delta G^{\ddagger}$) were calculated from the experimental rate constants ($k_{cat}$) using the equation $\Delta G^{\ddagger} = -RT \ln hk_{cat}/k_B T$, where $h$ denotes Planck's constant and $k_B$ Boltzmann's constant. Up to the posthydrolysis state, $(M^*\cdot ADP\cdot P_i)^{\ddagger}$, the profile was constructed from the reactant side using the following values: $K_1k_2 = 6.6 \times 10^5\ M^{-1}\ s^{-1}$ and $k_2 \approx 400\ s^{-1}$ from ref *37*; $k_{-2} = 2.3 \times 10^{-6}\ s^{-1}$ from ref *38*; and $K_{3a} = 0.4$, $k_{3a} = 350\ s^{-1}$, $k_{-3a} = 870\ s^{-1}$, $K_{3b} = 13$, $k_{3b} = 110\ s^{-1}$, and $k_{-3b} = 8.5\ s^{-1}$ from ref *39* (see also ref *40*). All values are taken from measurements performed on a *Dictyostelium discoideum* myosin II construct containing only a single tryptophan residue used as a fluorescence reporter. An exception is the value for $k_{-2}$ that was inferred from measurements of the ATP binding constant using rabbit myosin II ($K_1K_2 = 3.25 \times 10^{11}\ M^{-1}$, corresponding to a free energy $\Delta_R G_{1,2}$ of approximately $-15.4$ kcal/mol) (*41*, *42*). An upper bound for $k_{-2}$ estimated from displacement experiments with the ATP analogue AMP·PNP in *D. discoideum* is $\approx 0.02\ s^{-1}$. Although this value differs from the rabbit value of $k_{-2}$ by 4 orders of magnitude, the rabbit muscle myosin value is likely to be more appropriate since the differences between binding of ATP to muscle (rabbit) and non-muscle (*D. discoideum*) myosin II are expected to

[2] Throughout this paper, the *D. discoideum* myosin II numbering scheme is used.

be smaller than the differences between binding of ATP and AMP·PNP to non-muscle myosin II. The phosphate release steps (steps 4 and 5 in Figure 1A) are combined into a single step in Figure 1B. The overall rate-limiting step is the isomerization (step 4), for which a $k_4$ of 0.05 $s^{-1}$ was used (*43*). The corresponding barrier is 18.9 kcal/mol. The remainder of the profile was constructed from the product side up to $M^{\dagger}$·ADP+$P_i$ using the following values: $k_6 = 7.9\ s^{-1}$ and $k_{-6}/K_7 = 1.4 \times 10^6\ M\ s^{-1}$ from ref *37*. The formation of the collision complexes from either the reactant or the product sides of the profile occurs rapidly (*44*) and was assumed here to have a barrier of 2 kcal/mol.

To connect the two parts of the energy profile, a free energy of −7.4 kcal/mol was taken for the overall reaction (*45*, *46*). This corresponds to the free energy of ATP hydrolysis in solution under the conditions used for the myosin kinetic measurements (20 °C, 1 mM $MgCl_2$, and an ionic strength of ∼40 mM). The so-constructed profile shows an estimated $\Delta_R G_{4,5}$ value of 1.9 kcal/mol. This is within 0.5 kcal/mol of the experimental value of 1.4 kcal/mol corresponding to a $K_{4,5}$ of 0.085 M from ref *43*. This confirms the validity of the assumptions made in the construction of the profile and provides a rough estimate of the accuracy of the energy values given.

*Computational Setup.* The crystal structure of myosin complexed to the substrate analogue ADP·Be·$F_x$ in the C/C conformation (*47*) was used for the calculations. All protein atoms were included in the model. The beryllium atom was replaced with $P_\gamma$, and the three F atoms were replaced with O. Surface water molecules were removed, whereas internal water was kept, notably those water molecules located near the nucleotide. Since no attacking water molecule was resolved in the crystal structure, a water molecule was placed in the cavity adjacent to the $\gamma$-phosphate moiety. Hydrogens as required for the CHARMM (*48*) polar hydrogen MM force field (param 19/22) (*49*) were added using the HBUILD routine. At neutral pH, the predominant species of Mg·ATP is fully deprotonated (*45*). Thus, ATP was assumed to have a total charge of $-4e$ in the myosin active site. Standard protonation states were assumed for all titratable groups of the protein. No further modifications were made to the crystal structure.

The quantum mechanical region was chosen to consist of the triphosphate moiety of $ATP^{4-}$, the $Mg^{2+}$ ion, the two $Mg^{2+}$-coordinating crystal water molecules, the $Mg^{2+}$-coordinating side chains of Thr186 and Ser237, the attacking water molecule, an additional, crystallographically resolved water molecule next to the attacking water molecule (called here the "helper water"), and the side chains of Ser181 and Ser236. The valency at the QM/MM boundary was filled by adding five hydrogen link atoms. The total number of QM atoms is 57, of which 28 are non-hydrogen atoms. The QM and MM regions were linked as implemented in the CHARMM/GAMESS-US interface (*50*, *51*). The QM region, the P-loop, the Switch-1 loop, and the Switch-2 loop, augmented by all atoms within 12 Å of $P_\gamma$, were allowed to move freely during the reaction path calculations. This freely moving region was surrounded by a zone (all atoms between 12 and 20 Å from $P_\gamma$) in which the atoms were positionally restrained to their crystal structure positions, with force constants $k$ determined from the crystallographic temperature factors $B$ according to

$$k = \frac{4\pi^2 k_B T}{B} \quad (1)$$

where $k_B$ denotes Boltzmann's constant and $T$ the absolute temperature (300 K). The remaining protein atoms were kept fixed.

Table 1: Charge Scaling Factors for Residues Close to the QM Region

| residue *i* | $\lambda_{pept}$[a] | $\lambda_{side}$[b] | residue *i* | $\lambda_{pept}$[a] | $\lambda_{side}$[b] |
|---|---|---|---|---|---|
| Ser181 | 0.96 | na[c] | Ser237 | 0.90 | na[c] |
| Lys185 | 0.92 | 0.68 | Arg238 | 0.87 | 0.60 |
| Thr186 | 0.90 | na[c] | Ser456 | 0.93 | 1.02 |
| Asn233 | 0.91 | 0.95 | Gly457 | 0.85 | − |
| Ser236 | 0.94 | na[c] | Glu459 | 0.70 | 0.58 |

[a] Scaling factor for the peptide group formed by residues *i* and *i* + 1. [b] Scaling factor for the side chain of residue i. [c] The side chain is treated quantum mechanically.

Nonbonded interactions were truncated with a cubic switching function between 99 and 100 Å (equivalent to an infinite cutoff). Electrostatic solvent screening effects were approximated by scaling the partial atomic charges on all MM atoms with the Non-Uniform Charge Scaling (NUCS) procedure (*52*) in combination with a dielectric $\epsilon$ of 1. NUCS determines scaling factors to optimally reproduce with a Coulomb potential the electrostatic potential in solution determined by Poisson−Boltzmann calculations. Applying NUCS to the freely moving MM region allows the potential due to the charges of the free MM atoms to be described accurately throughout the whole unconstrained region. Partial atomic charges of atoms in the constrained and fixed regions were scaled to optimally reproduce the solution potential in the unconstrained region due to their charges. The rationale of this approach is to optimally represent the electrostatic potential acting on the QM and unconstrained MM atoms, the electrostatic potential in the constrained and fixed regions being less important in this context. The resulting scaling factors for the important residues interacting directly with the QM region are listed in Table 1.

Geometry optimization was performed using Hartree−Fock calculations (*53*) for the QM atoms with a 3-21G(d) basis set (*54*−*56*) and subsequently a 6-31G(d,p) (*57*, *58*) basis set. Point-energy calls were made on the structures optimized with HF/6-31G(d,p) using density-functional theory with the B3LYP functional (*59*−*61*) and 6-31+G-(d,p), a basis set that includes diffuse functions (*62*).

The choice of Hartree−Fock as the QM method implies significant energetic inaccuracies. The lack of electron correlation effects leads to an error on the order of 10 kcal/mol in the computation of barrier heights, even if large basis sets are used (*63*). Variation of as much as ∼15 kcal/mol has been found using various quantum chemical methods and basis sets for the reaction energy of a water exchange reaction of the much smaller $Sc(OH_2)_6^{3+}$ system (*64*). Although the use of density functional theory improves the accuracies, B3LYP calculations still show an average (maximum) error of ∼3 (∼20) kcal/mol in the calculation of heats of formation of a set of 148 molecules (*65*). Improved accuracy would be expected if, during geometry optimization, diffuse functions were included in the basis

set (*66*, *67*) and a quantum method including electron correlation effects was employed (*68*). This, however, exceeds currently available computational resources when combined with the refinement of complete reaction paths in a protein, which requires significantly more energy evaluations than a simple geometry optimization. This is reflected in the CPU time required by the present calculations: on eight 2.6 GHz processors, the QM/MM geometry optimization of a single protein structure at the HF/6-31G(d,p) level requires ~2 days, while the refinement of a path (composed of 10−30 structures) requires 2−4 months.

Although errors in the energy values are expected, structural results found to be common to the various levels of theory are likely to represent stable and reliable findings. The analyses in this work thus focus mostly on these method-invariant, structural aspects.

*Reactant and Product States.* To generate the reactant structure, the crystal structure prepared as described above was energy-minimized to a final root-mean-square gradient of 0.01 kcal mol$^{-1}$ Å$^{-1}$. The product state was generated starting from the minimized reactant structure: the linear combination of d{$P_\gamma$:$O_{\beta\gamma}$}−d{$P_\gamma$:$O^a$} interatomic distances (for the nomenclature of the atoms, see Figure 2A) was gradually changed during restrained minimizations to bring the system into a productlike geometry. The resulting structure was further energy-minimized (to a final rms gradient of 0.01 kcal mol$^{-1}$ Å$^{-1}$) after the restraints were released. The different product states for the direct, Ser181, and Ser236 paths were generated by a manual shift of the corresponding protons and subsequent energy minimization. Because the link-atom scheme was used, geometric distortions may occur at the QM/MM boundaries. Here, the deviations between the QM/MM bond lengths (angles) and the corresponding MM bond lengths (angles), as parametrized for CHARMM, are less than 0.15 Å (5°), small enough to be tolerated. Moreover, no geometric changes at the QM/MM boundaries were observed throughout the paths. Thus, these small distortions cancel out when relative energies are computed.

*Path Calculations and Analysis.* Minimum-energy pathways of the reaction paths were computed with the conjugate peak refinement (CPR) method (*69*), as implemented in the TReK module of CHARMM. CPR has been used to determine the functional mechanisms of several proteins, such as catalysis by the prolyl-isomerase FKBP (*70*), proton transfer in bacteriorhodopsin (*71*), chloride pumping in halorhodopsin (*72*), and the recovery stroke in myosin (*12*). The combination of ab initio QM/MM techniques with CPR was used previously to investigate the ATP hydrolysis step in myosin and has been shown to be capable of distinguishing between the hydrolysis-incompetent C/O and hydrolysis-competent C/C myosin conformations (*35*). CPR has an advantage in that it does not require the definition of a reaction coordinate to drive the reaction. Instead, it starts from an initial guess of the whole path, which it refines until a series of structures are obtained that connect the reactant and product states in a continuous fashion. The energy peaks along this refined path are the transition states [i.e., the first-order saddle-point(s) of the high-dimensional energy surface, here ~6000-dimensional, corresponding to 3 times the number of unconstrained atoms], the structures of which are accurately determined. Progress of the reaction is measured here by the intrinsic reaction coordinate, which is the curvilinear distance along the path, computed as the sum $\lambda$ of the rms coordinate difference between pairs of adjacent structures along the path. $\lambda$ is normalized so that a $\lambda$ of 1 corresponds to the product state.

Initial path guesses were obtained by linear interpolation in Cartesian coordinates between the reactant and product structures while passing through transient structures that were generated by manually shifting the moving hydrogens from the reactant to the product structures to prevent steric clashes in the initial path. The initial paths were optimized by CPR using first HF/3-21G(d) for the QM region. From each resulting minimum-energy path, the transition state and its two neighboring path points were then used as intermediates in an initial path further optimized by CPR with HF/6-31G-(d,p) for the QM region. Along this refined path, QM/MM single energy evaluations were carried out with B3LYP/6-31+G(d,p).

The quantum mechanical contribution to the total energy, $\Delta E_{QM}$, comprises both the energy of the quantum region, $\Delta E_{QM}^{QM}$, and the electrostatic interaction energy between the quantum atoms and the remaining proteins atom, $\Delta E_{elec}^{QM/MM}$, which also includes polarization effects. $\Delta E_{QM}^{QM}$ is given by the quantum mechanical energy contribution to the total energy from QM/MM single-point energy evaluations along the refined path after all partial atomic charges on MM atoms are set to zero. $\Delta E_{elec}^{QM/MM}$ is then calculated as the difference

$$\Delta E_{elec}^{QM/MM} = \Delta E_{QM} - \Delta E_{QM}^{QM} \quad (2)$$

The electrostatic contribution from individual residues of the Switch-1 loop, the Switch-2 loop, and the P-loops was analyzed by recomputing the energy difference between stationary points of the paths, $\Delta E_{tot}$, after the charges on a given residue X had been set to zero, $\Delta E_{tot}^{q(X)=0}$.

$$\Delta E_{elec}^{X} = \Delta E_{tot} - \Delta E_{tot}^{q(X)=0} \quad (3)$$

The difference gives the electrostatic contribution to the barrier height or to the reaction energy due to the charges on residue X (*73*). To analyze charge shifts during the reaction, Mulliken population analyses (*74*) were carried out at the stationary points.

## RESULTS

### *Energy Profiles*

In Table 2 are listed the barrier heights and reaction energies for the three pathways at different levels of theory. The choice of the QM method strongly influences the barrier height, which varies between 26 and 51 kcal/mol. This indicates that quantum methods of a level higher than that used here may be required to obtain reliable absolute energy barriers. Remarkably, however, at any given level of theory, the barrier heights of the three mechanisms are very close to each other. Thus, the three activation mechanisms are, within error, likely to be equally populated.

The energy profiles along the direct, Ser181, and Ser236 paths obtained with HF/3-21G(d) or HF/6-31G(d,p) are shown in Figure 3. In all three activation mechanisms, the shapes of the energy profiles calculated with HF/3-21G(d)//

Table 2: Barrier Heights and Reaction Energies in Kilocalories per Mole

| | barrier height | | |
|---|---|---|---|
| | direct | Ser181 | Ser236 |
| HF/3-21G(d)//HF3-21G(d) | 26.1 | 29.0 | 28.1 |
| HF/6-31G(d,p)//HF/6-31G(d,p) | 50.9 | 45.6 | 51.0 |
| B3LYP/6-31+G(d,p)//HF/6-31G(d,p) | 41.1 | 38.0 | 41.3 |
| | reaction energy | | |
| | direct | Ser181 | Ser236 |
| HF/3-21G(d)//HF3-21G(d) | 17.1 | 6.9 | 20.7 |
| HF/6-31G(d,p)//HF/6-31G(d,p) | 25.9 | 9.5 | 28.0 |
| B3LYP/6-31+G(d,p)//HF/6-31G(d,p) | 27.6 | 10.8 | 29.7 |

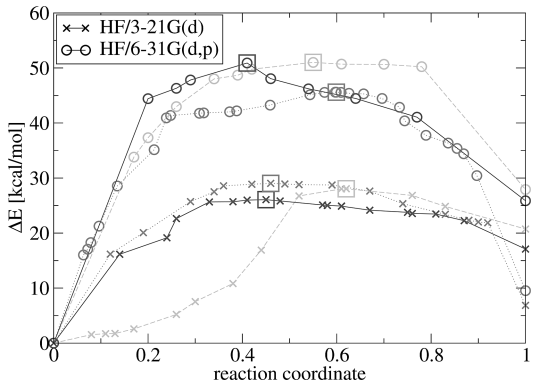


FIGURE 3: Energy profiles along the direct (solid lines), Ser181 (dotted lines), and Ser236 (dashed lines) paths, optimized with either the HF/3-21G(d) (×) or the HF/6-31G(d,p) (○) QM method. Saddle points are indicated with squares. The reaction coordinate is the normalized sum taken along the path of rms changes in all atom coordinates ($\lambda$, see Methods).

HF/3-21G(d) and B3LYP/6-31+G(d,p)//HF/3-21G(d) differ significantly (data not shown). In particular, the saddle point on the HF/3-21G(d)//HF/3-21G(d) surface is no longer the highest-energy point on the B3LYP/6-31+G(d,p)//HF/3-21G-(d) surface. This indicates that the geometries optimized with HF/3-21G(d) are different from the geometries that would be found when using larger basis sets. Thus, the 3-21G(d) basis set is not sufficiently accurate for describing the geometries along the ATP hydrolysis reaction pathway in myosin. Therefore, the HF/3-21G(d)-refined paths are not further considered here. In contrast, the B3LYP postprocessing does not alter the shapes of the paths optimized with HF/6-31G(d,p), and the saddle points remain the highest-energy points within the error of the method. This indicates that the 6-31G(d,p) basis set with Hartree−Fock geometry optimization provides reasonable structural accuracy.

### *Geometries along the Paths*

*Reactant State.* An overlap of the nucleotide binding site of the energy-minimized reactant state [using HF/6-31G(d,p) for the QM region] with the unminimized crystal-like structure shows that the protein structure remained largely unchanged upon minimization. The internal geometry of the triphosphate moiety of ATP in the protein is similar to that found with density functional theory quantum dynamics of $Mg^{2+}$-coordinated methyl triphosphate ($Mg{\cdot}MTP_{aq}$) in solution (*75*) (Table 3). The distance between a phosphorus and its terminal oxygens varies between 1.49 and 1.52 Å and is thus close to the range observed in $Mg{\cdot}MTP_{aq}$ (1.51−1.55 Å). Minimization introduces an asymmetry by elongating the $\{P_\gamma-O_{\beta\gamma}\}$ bond (to 1.68 Å) relative to the $\{P_\beta-O_{\beta\gamma}\}$ bond (1.60 Å). The $\{P_\gamma-O_{\beta\gamma}-P_\beta\}$ angle is 126.6°, similar to the value of 128.3° for $Mg{\cdot}MTP_{aq}$. The $\{O_{\beta\gamma}-P_\gamma-O_\gamma\}$ angles vary between 103.2° and 106.7° and are thus somewhat smaller than the angle corresponding to a tetrahedral arrangement (109.5°). Thus, the enzymatic environment slightly distorts the $\gamma$-phosphate moiety of ATP into the direction of a trigonal bipyramidal transition-state configuration in which the $\{O_{\beta\gamma}-P_\gamma-O_\gamma\}$ angle would be 90°.

In both the minimized and crystal structures, an almost perfect octahedron is observed for the $Mg^{2+}$ coordination sphere, as observed for $Mg{\cdot}MTP_{aq}$ in solution (*75*). Thus, the enzyme environment does not introduce significant changes into the $Mg^{2+}$ coordination as compared to an aqueous environment.

The attacking water ($H_2O^a$ in Figure 2B) forms hydrogen bonds to the carbonyl oxygen of Ser237 ($d\{O^a-O^{S237}\}$ distance of 2.81 Å) and to $O_{\gamma2}$ of the $\gamma$-phosphate moiety of ATP ($d\{O^a-O_{\gamma2}\} = 3.06$ Å). The side chains of both Ser181 and Ser236 also form hydrogen bonds to $O_{\gamma2}$ with the following distances: $d\{O^{S181}-O_{\gamma2}\} = 2.77$ Å and $d\{O^{S236}-O_{\gamma2}\} = 2.86$ Å. The helper water is hydrogen bonded to the side chains of Ser181 ($d\{O^h-O^{S181}\} = 2.96$ Å) and Ser236 ($d\{O^h-O^{S236}\} = 3.13$ Å). Altogether, this forms a hydrogen bond network around the $\gamma$-phosphate which favors multiple pathways for proton transfer and positions the proton donors corresponding to the three paths studied here for efficient transfer of a proton onto $O_{\gamma2}$. These paths are described in the following sections and can best be understood by watching the molecular movies that can be downloaded from http://www.iwr.uni-heidelberg.de/groups/biocomp/fischer.

*Direct Path.* If one starts from the reactant structure (reaction coordinate $\lambda = 0.00$), the first event in the direct path is the activation of the attacking water by proton transfer of the $H_2{}^a$ proton from the attacking water to $O_{\gamma2}$ of ATP, which is completed at $\lambda = 0.29$. The resulting $O^aH^-$ hydroxide then attacks $P_\gamma$, this attack resulting in the rate-limiting transition state (TS) at $\lambda = 0.41$, which exhibits almost trigonal bipyramidal geometry (Figure 4A). When a fully trigonal bipyramidal structure (as characterized by an improper dihedral angle $a\{P_\gamma-O_{\gamma1}-O_{\gamma2}-O_{\gamma3}\}$ of 0°) is reached, at $\lambda = 0.46$, the distances to the attacking oxygen ($d\{P_\gamma-O^a\} = 1.81$ Å) and to the leaving oxygen ($d\{P_\gamma-O_{\beta\gamma}\} = 1.84$ Å) are nearly equal. Up to the TS at $\lambda = 0.41$ (Figure 4A), the $Mg^{2+}$ coordination angle ($\{O_{\gamma3}-Mg-O_{\beta2}\}$) remains approximately 90° and the coordination of $Mg^{2+}$ by Ser237 on the Switch-1 loop is maintained (the $\{Mg-O_\gamma^{S237}\}$ distance stays at 2.2 Å). This changes during the decay of the TS into the product (Figure 4B), where the $\{O_{\gamma3}-Mg-O_{\beta2}\}$ angle widens to 125°, pulling the $Mg^{2+}$ between the $\beta$-phosphate and the leaving $\gamma$-phosphate and provoking an increase in the $\{Mg-O_\gamma^{S237}\}$ distance to 3.6 Å. This increase is due to $Mg^{2+}$ and $O_\gamma^{S237}$ moving in opposite directions. This is very important because it breaks the coordination bond between $Mg^{2+}$ and the Switch-1 loop in the product state (Figure 4B), thereby weakening a strong interaction that keeps Switch-1 closed over the nucleotide.

Table 3: Geometric[a] Characteristics of the QM Region Optimized with HF/6-31G(d,p)

| | *R* | Mg·MTP$_{aq}$[b] | TS$_{direct}$ | TS$_{Ser181}$ | TS$_{Ser236}$ | P$_{direct}$ | P$_{Ser181}$ | P$_{Ser236}$ |
|---|---|---|---|---|---|---|---|---|
| {$P_\gamma-O^a$} | 3.56 | − | 2.18 | 2.18 | 2.18 | 1.61 | 1.60 | 1.62 |
| {$P_\gamma-O_{\gamma1}$} | 1.50 | 1.51−1.55 | 1.49 | 1.49 | 1.49 | 1.48 | 1.48 | 1.48 |
| {$P_\gamma-O_{\gamma2}$} | 1.50 | 1.51−1.55 | 1.60 | 1.59 | 1.60 | 1.59 | 1.58 | 1.59 |
| {$P_\gamma-O_{\gamma3}$} | 1.52 | 1.51−1.55 | 1.51 | 1.51 | 1.51 | 1.50 | 1.51 | 1.50 |
| {$P_\gamma-O_{\beta\gamma}$} | 1.68 | 1.70 | 1.73 | 1.73 | 1.73 | 3.30 | 3.24 | 3.28 |
| {$P_\beta-O_{\beta\gamma}$} | 1.60 | 1.62 | 1.58 | 1.57 | 1.58 | 1.50 | 1.51 | 1.50 |
| {$P_\beta-O_{\beta1}$} | 1.49 | 1.51−1.55 | 1.49 | 1.49 | 1.49 | 1.50 | 1.50 | 1.50 |
| {$P_\beta-O_{\beta2}$} | 1.50 | 1.51−1.55 | 1.50 | 1.50 | 1.50 | 1.54 | 1.53 | 1.54 |
| {$P_\gamma-O_{\beta\gamma}-P_\beta$} | 126.6 | 128.3 | 128.2 | 130.5 | 128.2 | 124.8 | 116.7 | 124.2 |
| {$O_{\beta\gamma}-P_\gamma-O_{\gamma1}$} | 106.7 | − | 101.9 | 101.2 | 101.8 | 83.4 | 86.8 | 84.5 |
| {$O_{\beta\gamma}-P_\gamma-O_{\gamma2}$} | 103.8 | − | 87.91 | 85.8 | 88.0 | 69.8 | 53.0 | 69.3 |
| {$O_{\beta\gamma}-P_\gamma-O_{\gamma3}$} | 103.2 | − | 98.2 | 98.6 | 98.2 | 71.2 | 82.2 | 71.4 |
| {$O_{\beta\gamma}-P_\gamma-O^a$} | 157.1 | − | 161.2 | 163.2 | 161.2 | 163.1 | 151.3 | 162.0 |
| {$O^a-P_\gamma-O_{\gamma1}$} | 72.9 | − | 90.5 | 89.0 | 90.5 | 111.0 | 111.1 | 110.9 |
| {$O^a-P_\gamma-O_{\gamma2}$} | 58.9 | − | 73.7 | 77.5 | 73.7 | 95.5 | 98.4 | 95.1 |
| {$O^a-P_\gamma-O_{\gamma3}$} | 97.7 | − | 87.6 | 88.0 | 87.5 | 108.1 | 108.7 | 107.9 |
| {$P_\gamma-O_{\gamma1}-O_{\gamma2}-O_{\gamma3}$} | 28.7 | − | 11.9 | 10.5 | 11.9 | −28.4 | −30.6 | −27.9 |
| {$O^a-H^a_2$} | 0.95 | − | 1.66 | 1.89 | 0.94 | 2.34 | 3.81 | 0.96 |
| {$H^a_2-O_{\gamma2}$} | 2.14 | − | 0.96 | 2.88 | 3.16 | 0.96 | 3.59 | 3.26 |
| {$H^a_2-O^h$} | 3.85 | − | 3.45 | 0.96 | 4.70 | 2.05 | 0.95 | 4.54 |
| {$O^h-H^h_2$} | 0.95 | − | 0.95 | 1.92 | 0.95 | 0.95 | 1.98 | 0.95 |
| {$H^h_2-O_\gamma^{S181}$} | 2.05 | − | 2.13 | 0.95 | 2.13 | 2.03 | 0.95 | 2.05 |
| {$O_\gamma^{S181}-H_\gamma^{S181}$} | 0.96 | − | 0.95 | 2.89 | 0.95 | 0.95 | 3.30 | 0.95 |
| {$H_\gamma^{S181}-O_{\gamma2}$} | 1.81 | − | 1.94 | 0.94 | 1.94 | 2.07 | 0.98 | 2.07 |
| {$O^a-H^a_1$} | 0.95 | − | 0.94 | 0.94 | 1.64 | 0.96 | 0.96 | 2.07 |
| {$H^a_1-O_\gamma^{S236}$} | 2.89 | − | 3.12 | 3.08 | 0.98 | 3.33 | 3.17 | 0.95 |
| {$O_\gamma^{S236}-H_\gamma^{S236}$} | 0.96 | − | 0.98 | 0.98 | 2.83 | 0.95 | 0.95 | 2.96 |
| {$H_\gamma^{S236}-O_{\gamma2}$} | 1.90 | - | 2.90 | 3.02 | 0.96 | 2.39 | 2.10 | 0.96 |
| {$Mg-O_{\gamma3}$} | 1.97 | 2.15 | 1.99 | 2.00 | 1.99 | 2.03 | 1.99 | 2.04 |
| {$Mg-O_{\beta2}$} | 2.05 | 2.15 | 2.04 | 2.03 | 2.04 | 1.91 | 1.91 | 1.91 |
| {$Mg-O^{w1}$} | 2.10 | − | 2.09 | 2.09 | 2.09 | 2.03 | 2.05 | 2.03 |
| {$Mg-O^{w2}$} | 2.10 | − | 2.10 | 2.11 | 2.10 | 2.12 | 2.12 | 2.11 |
| {$Mg-O_{\gamma1}^{T186}$} | 2.08 | − | 2.09 | 2.10 | 2.09 | 2.20 | 2.13 | 2.18 |
| {$Mg-O_\gamma^{S237}$} | 2.23 | − | 2.24 | 2.23 | 2.24 | 3.58 | 3.45 | 3.50 |
| {$O_{\gamma3}-Mg-O_{\beta2}$} | 91.1 | 90.0 | 90.7 | 93.3 | 90.7 | 125.2 | 119.8 | 122.1 |

[a] Distances in angstroms and angles in degrees. [b] Geometric data for Mg·MTP (methyl triphosphate) in aqueous solution as determined from Car−Parrinello molecular dynamics (*75*).

*Ser181 Path.* In the beginning of the Ser181 path, up to $\lambda = 0.21$, the attacking water reorients so that it is able to transfer its $H_2^a$ proton onto the helper water. In the same path segment ($\lambda = 0.10$ to $\lambda = 0.21$), Ser181 transfers its $H_\gamma^{S181}$ proton to $O_{\gamma2}$ of the ATP. Directly after the $H_\gamma^{S181}$ proton has been transferred, it points toward the side chain of Ser181, as expected. The second proton transfer event, in which the helper water transfers its $H_2^h$ onto the side chain of Ser181, occurs between $\lambda = 0.21$ and $\lambda = 0.25$. This proton remains oriented toward the oxygen, $O^h$, from which it originates, throughout the rest of the path. A third proton transfer occurs between $\lambda = 0.37$ and $\lambda = 0.46$. In this path segment, the attacking water transfers its $H_2^a$ onto the helper water oxygen, $O^h$.

Meanwhile, the $O_{\gamma2}H_\gamma^{S181}$ group rotates so that the proton points toward the attacking water oxygen at $\lambda = 0.39$ and then toward the helper water oxygen, $O^h$, at $\lambda = 0.60$ (see the molecular movies). Up to $\lambda \approx 0.70$, $H_2^a$ keeps its orientation toward $O^a$, whereas the helper water reorients in the final part of the path such that in the product state $H_2^a$ mediates a hydrogen bond between the helper water and the side chain of Ser236 (Figure 4F). Between $\lambda = 0.66$ and $\lambda = 1.0$, the $O_{\gamma2}H_\gamma^{S181}$ group rotates back in an almost 180° rotation so that in the product state it mediates a hydrogen bond between $O_{\gamma2}$ of the $P_i$ moiety and $O_{\beta\gamma}$ of the ADP (see Figure 4F). This hydrogen bond to the anionic ADP is more favorable than the hydrogen bond made by $P_i$ in the product states of the direct path or of the Ser236 path (to the helper water; see Figure 4C,I). This is the reason the product of the Ser181 path has a lower energy (Figure 3).

The transition state at $\lambda = 0.60$ is of near-trigonal bipyramidal geometry (Figure 4D). At $\lambda = 0.66$, the trigonal bipyramidal geometry is reached (improper dihedral {$P_\gamma-O_{\gamma1}-O_{\gamma2}-O_{\gamma3}$} angle of zero with distances to the incoming and leaving oxygens of 1.92 ($d${$P_\gamma-O^a$}) and 1.88 Å ($d${$P_\gamma-O_{\beta\gamma}$}), respectively. As observed in the direct path, up to the TS at $\lambda = 0.60$, the {$O_{\gamma3}-Mg-O_{\beta2}$} angle remains below 93° and the {$Mg-O_\gamma^{S237}$} distance stays around 2.2 Å. During decay to the product (after $\lambda = 0.66$), the {$O_{\gamma3}-Mg-O_{\beta2}$} angle widens (final value of 120°) and the {$Mg-O_\gamma^{S237}$} distance increases to 3.4 Å (Figure 4E), due to the simultaneous motion of $Mg^{2+}$ and $O_\gamma^{S237}$. As in the direct path, this increase in the {$Mg-O_\gamma^{S237}$} distance weakens the link between the Switch-1 loop and the $Mg^{2+}$.

As in the direct path, the attacking water is activated before the resulting $O^aH^-$ nucleophile attacks the $\gamma$-phosphate moiety of ATP, thus forming the rate-limiting transition state. The activation relay involving the helper water and Ser181 is described above as being sequential, as is indeed found in the CPR-optimized path. However, this implies that intermediate states separated by barriers corresponding to each proton transfer event should have been located as minima on the potential energy surface, which is not the case.

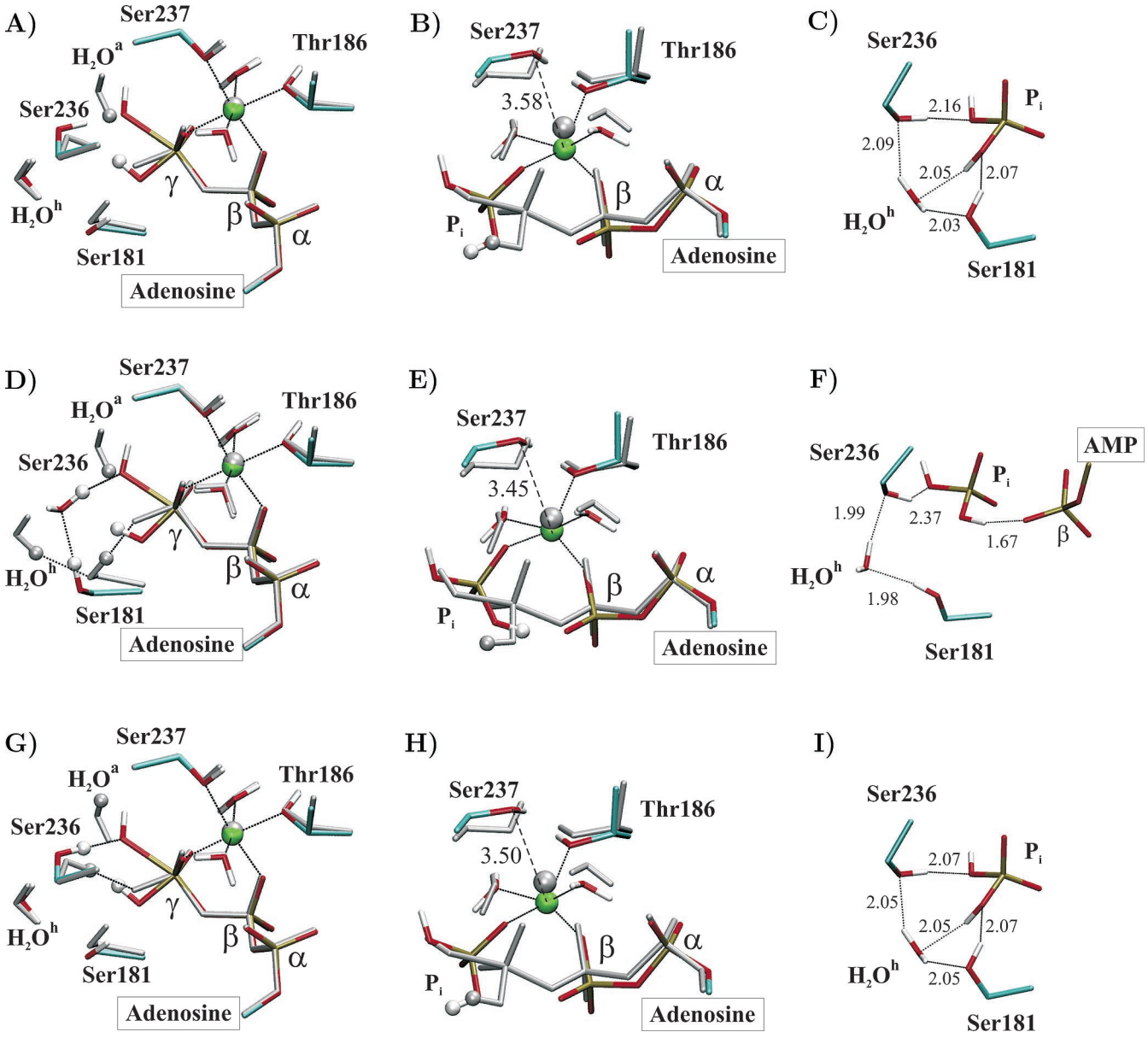


FIGURE 4: In the left column, the rate-limiting transition states optimized with HF/6-31G(d,p) (color) are overlapped with the reactant state (gray). In the middle column, the product states (color) are overlapped with the transition state (gray structure, same as in the left column). In the right column, the hydrogen bonding network around $P_i$ in the product state is shown. (A−C) Direct path. (D−F) Ser181 path. (G−I) Ser236 path.

Proton transfers occur here from a neutral species to an anionic species, thereby leading to an effective transport of a hydroxide anion through the myosin active site. The mechanism of this transport may be similar to the mechanism of transport of hydrated hydroxide in bulk water that has been shown to be sequential via energy barriers of approximately 3 kcal/mol (*76*). Those barriers are much smaller than the overall barrier and therefore are unresolved in this energy profile.

*Ser236 Path.* The first event in the Ser236 path, between $\lambda = 0.00$ and $\lambda = 0.34$, is the proton transfer of the $H_\gamma^{S236}$ proton from the side chain of Ser236 onto $O_{\gamma 2}$ of ATP. Simultaneously, the attacking water reorients into a position that is optimal for the transfer of its $H_1{}^a$ proton to the side chain of Ser236. This second proton transfer occurs between $\lambda = 0.39$ and $\lambda = 0.55$, where the transition state of nearly trigonal bipyramidal geometry is reached (Figure 4G). The trigonal bipyramidal structure is reached between $\lambda = 0.61$ and $\lambda = 0.70$ (the $\{P_\gamma{-}O_{\gamma 1}{-}O_{\gamma 2}{-}O_{\gamma 3}\}$ improper angle is $0 \pm 5°$); the distance to the attacking oxygen ($\{P_\gamma{-}O^a\}$) decreases from 2.0 to 1.8 Å, and the distance to the leaving oxygen ($\{P_\gamma{-}O_{\beta\gamma}\}$) increases from 1.8 to 2.1 Å. As was the case for the direct and Ser181 paths, the $\{O_{\gamma 3}{-}Mg{-}O_{\beta 2}\}$ angle remains close to 90° and the $\{Mg{-}O_\gamma^{S237}\}$ distance stays at 2.2 Å up to the TS at $\lambda = 0.55$. When the TS decays, the $\{O_{\gamma 3}{-}Mg{-}O_{\beta 2}\}$ angle then widens to its final value of 122° and the $\{Mg{-}O_\gamma^{S237}\}$ distance increases to 3.5 Å in the product state (Figure 4H), again breaking the link between Switch-1 and the $Mg^{2+}$.

*Transition State.* The three paths share common behavior. Figure 5A shows the variation of improper dihedral angle $\{P_\gamma{-}O_{\gamma 1}{-}O_{\gamma 2}{-}O_{\gamma 3}\}$ that measures the pyramidality at $P_\gamma$ (a positive value corresponds to the pyramidal configuration of the reactant, pyramidal inversion at $P_\gamma$ yielding a negative value characteristic for the product configuration). If one

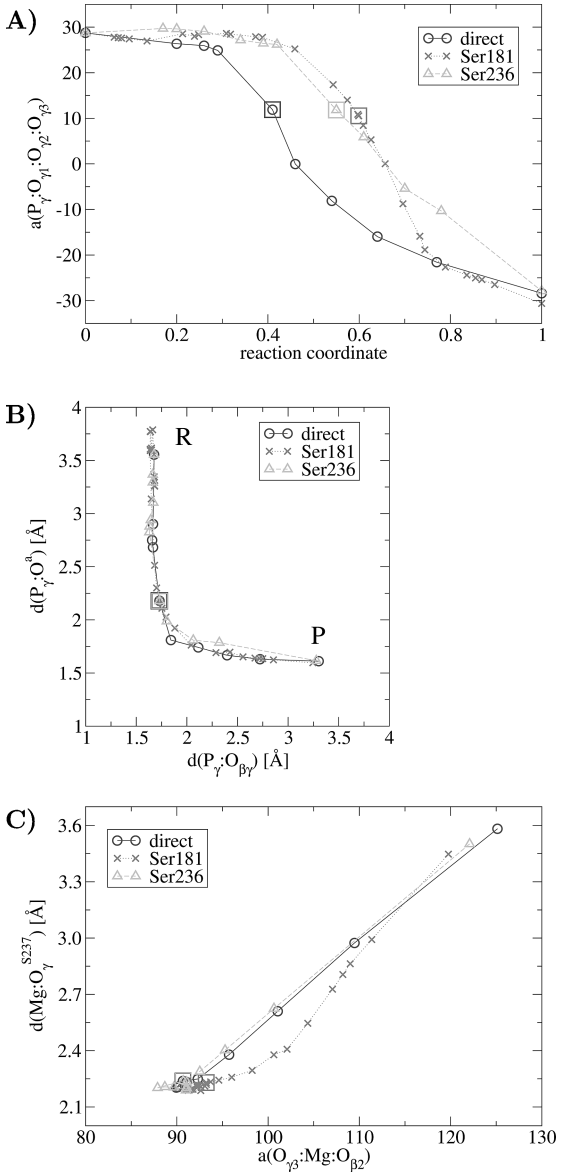


FIGURE 5: (A) Improper angle ($\{P_\gamma-O_{\gamma1}-O_{\gamma2}-O_{\gamma3}\}$) in degrees measuring the pyramidal configuration at $P_\gamma$ plotted along the three paths [the direct (solid lines), Ser181 (dotted lines), and Ser236 (dashed lines) paths, optimized with HF/6-31G(d,p)]. Same reaction coordinate ($\lambda$) as in Figure 3. Transition states are denoted with squares. (B) Distance between $P_\gamma$ and the attacking oxygen ($d\{P_\gamma-O^a\}$) vs distance between $P_\gamma$ and the leaving oxygen ($d\{P_\gamma-O_{\beta\gamma}\}$) for the three paths. (C) Distance $d\{Mg-O_\gamma^{S237}\}$ vs the $\{O_{\gamma3}-Mg-O_{\beta2}\}$ angle in degrees for the three paths.

starts from nearly perfect pyramidality ($\{P_\gamma-O_{\gamma1}-O_{\gamma2}-O_{\gamma3}\}$ angle of 28.7°), the pyramidal inversion occurs abruptly (sigmoidal curve). In each of the three paths, the transition state has a $\{P_\gamma-O_{\gamma1}-O_{\gamma2}-O_{\gamma3}\}$ angle close to 10°, i.e., near the planar configuration (characterized by an angle of 0°).

A convenient way of visualizing the relative associative or dissociative character of the reaction is to plot the $\{P_\gamma-O^a\}$ distance between $P_\gamma$ and the incoming oxygen versus the $\{P_\gamma-O_{\beta\gamma}\}$ distance between $P_\gamma$ and the leaving $\beta\gamma$-bridge oxygen (Figure 5B). In all three paths, the $\{P_\gamma-O^a\}$ distance is shortened first, followed by elongation of the $\{P_\gamma-O_{\beta\gamma}\}$ distance. Thus, all three water activation mechanisms lead to a clearly associative reaction route. The pentacovalent state was not found to be a stable intermediate. Remarkably, the transition states of the three paths have the same distance pairs: $d\{P_\gamma-O^a\} = 2.18$ Å and $d\{P_\gamma-O_{\beta\gamma}\} = 1.73$ Å (Figure 2C).

*Product State.* Panels B, E, and H of Figure 4 show the product conformation of the direct, Ser181, and Ser236 paths. In all three products, the $P_i$ is clearly separated from the ADP and the $Mg^{2+}$ coordination sphere has broken up (comprising only five ligands rather than six in the reactant). This is due to an elongation of the $\{Mg-O_\gamma^{S237}\}$ distance that results from the breaking of the coordination bond between the $Mg^{2+}$ and the Switch-1 loop. Figure 5C plots the $\{Mg-O_\gamma^{S237}\}$ distance versus the $\{O_{\gamma3}-Mg-O_{\beta2}\}$ angle. The widening of this angle upon decay of the bipyramidal transient states is linearly correlated with the increase in distance and thus breakage of the $\{Mg-O_\gamma^{S237}\}$ coordination bond. This weakens the connection between the Switch-1 loop and the $Mg^{2+}$ coordination sphere, thus favoring a subsequent opening of the Switch-1 loop, which is expected to occur concurrently with actin binding (see Discussion).

The hydrogen bonding network is identical in the products of the direct and Ser236 paths (Figure 4, panels C and I, respectively), which therefore have similar reaction energies (see Table 2). The product of the Ser181 path is significantly lower in energy, due to the fact that the $\gamma$-phosphate (i.e., inorganic phosphate, $P_i^-$) donates a hydrogen bond to the negatively charged $\beta$-phosphate of $ADP^{3-}$ (Figure 4F), rather than with the neutral "helper" water ($H_2O^h$) in the products of the other two paths. A small rearrangement of the hydrogen bond network allows the products of the direct and Ser236 paths to adopt the lower-energy conformation of the Ser181 path, which thus is the preferred model for the actual product state for all three paths. Other than indicating this variation in the hydrogen bonding pattern for the product state, the difference in reaction energies between the paths is of no significance.

### *Energy Decomposition*

Further insight into the energetics along the reaction paths is gained by decomposing the total energies into their contributing terms. These are the bonded, van der Waals, MM electrostatic interaction, positional constraint (*B*-factor), and quantum energy terms. The quantum energy includes both the energy of the QM region and that of its electrostatic interactions with the MM region. Panels A and B of Figure 6 show this dissection for the direct and Ser181 paths, respectively. The shape of the total energy profile and the barrier at the transition state are dominated by the QM energy. The largest contribution to the barrier from the MM terms is the electrostatics for the direct path (5.6 kcal/mol) and the van der Waals contributions for the Ser181 path (3.3 kcal/mol).

In the product state, the largest contributions come from the MM electrostatics and van der Waals terms that are unfavorable by 13.9 and 8.1 kcal/mol, respectively, in the direct path (in the Ser181 path, these two terms contribute 7.8 kcal/mol each). Thus, the intraprotein MM energy terms somewhat destabilize the product state. In the direct path (and in the Ser236 path), this destabilization is not offset by the QM energy (which contributes only 0.3 or 2.0 kcal/mol with HF or B3LYP), thus resulting in an unfavorable overall reaction energy of 27.6 kcal/mol. In contrast, in the Ser181 path, the QM term stabilizes the product state (by −10.1 or

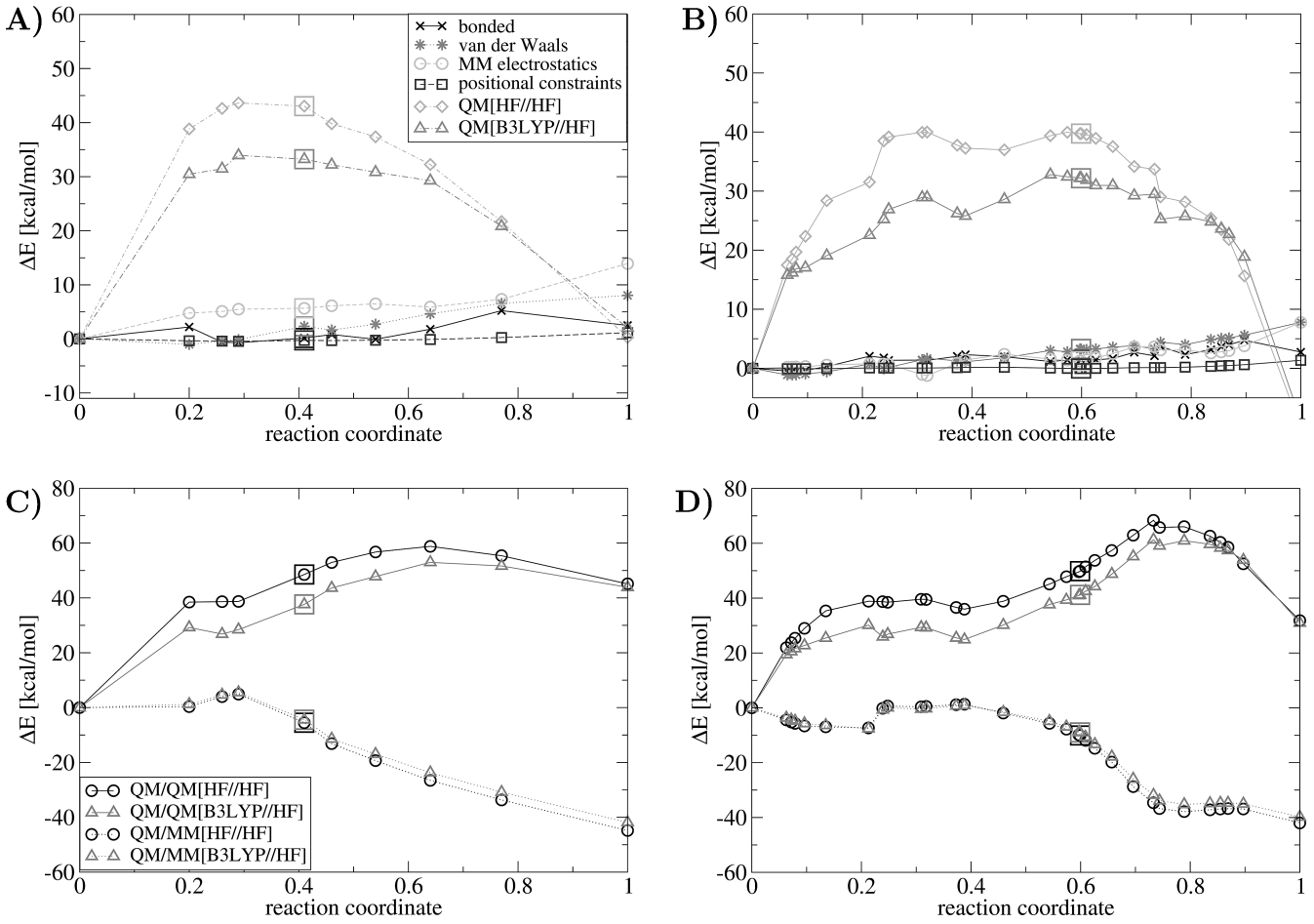


FIGURE 6: Energy decomposition along the reaction paths. (A and B) Dissection of the total energy into all its contributing terms [in kilocalories per mole, pathways optimized with HF/6-31G(d,p)]. (C and D) Decomposition of the QM energy term of the top panels into (1) the energy of the QM region itself ($\Delta E_{QM}^{QM}$) and (2) the electrostatic interaction between the QM and MM regions ($\Delta E_{elec}^{QM/MM}$) (see Methods). The HF//HF curves plot the HF/6-31G(d,p) energy and the B3LYP//HF curves the energy from energy evaluation with B3LYP/6-31+G(d,p). (A and C) Direct path (decomposition of the Ser236 path is very similar). (B and D) Ser181 path. Same reaction coordinate ($\lambda$) as in Figure 3. The transition states are denoted with squares.

−8.8 kcal/mol with HF or B3LYP, respectively), due to formation of the hydrogen bond between $P_i$ and ADP described above.

The positional constraint energy stays close to zero in all three paths. This indicates that, throughout the course of the reaction, the regions distant from the active site are not significantly distorted and that all protein motions necessary for the reaction are indeed confined to the freely moving region (see Methods). This shows that the size of freely moving region has been made large enough to accommodate the local structural rearrangements that are required during ATP hydrolysis in myosin.

A further dissection of the QM energy into the quantum energy of the quantum region ($\Delta E_{QM}^{QM}$) and the QM/MM electrostatic interaction ($\Delta E_{elec}^{QM/MM}$) for the direct path is shown in Figure 6C. $\Delta E_{QM}^{QM}$ increases up to a maximum at $\lambda = 0.64$, with values of 58.5 and 53.0 kcal/mol with HF and B3LYP, respectively. This is comparable to the barrier height of ∼50 kcal/mol that has been reported for methyl triphosphate hydrolysis in the gas phase in the presence of one explicit water molecule (*77*). In the product state, $\Delta E_{QM}^{QM}$ equals ∼44−45 kcal/mol. This large unfavorable quantum energy is due to the repulsion of the inorganic phosphate and the ADP that are both negatively charged. The unfavorable energy is essentially completely compensated by the favorable QM/MM electrostatic interaction energy ($\Delta E_{elec}^{QM/MM}$) that stabilizes the product by −44.8 kcal/mol relative to the reactant for HF (or −41.9 kcal/mol for B3LYP). The origin of this compensation is discussed below. Similar observations were made for the dissection of the Ser236 path (not shown). Figure 6D shows the corresponding decomposition for the Ser181 path. As in the direct path, $\Delta E_{QM}^{QM}$ increases initially, reaching a maximum of 68.4 or 61.3 kcal/mol at $\lambda = 0.73$ for HF or B3LYP, respectively. In the product state, $\Delta E_{QM}^{QM}$ equals ∼31−32 kcal/mol and thus is roughly 10 kcal/mol less unfavorable than in the product state of the direct path, due to the hydrogen bond between the inorganic phosphate and the ADP present in the product of the Ser181 path (see above). $\Delta E_{elec}^{QM/MM}$ is favorable by −42.0 kcal/mol with HF (or −39.8 kcal/mol with B3LYP). Thus, the QM/MM electrostatic interactions with the protein stabilize the product state of the substrate by an equal amount in the direct and Ser181 paths.

### *Electrostatic Interactions*

Figure 7 (left panels) shows the electrostatic energy contributions to the barrier height from individual residues of the P-loop, the Switch-1 loop, and the Switch-2 loop. Of particular interest is the contribution of the salt bridge between Arg238 and Glu459 that connects the Switch-1 and

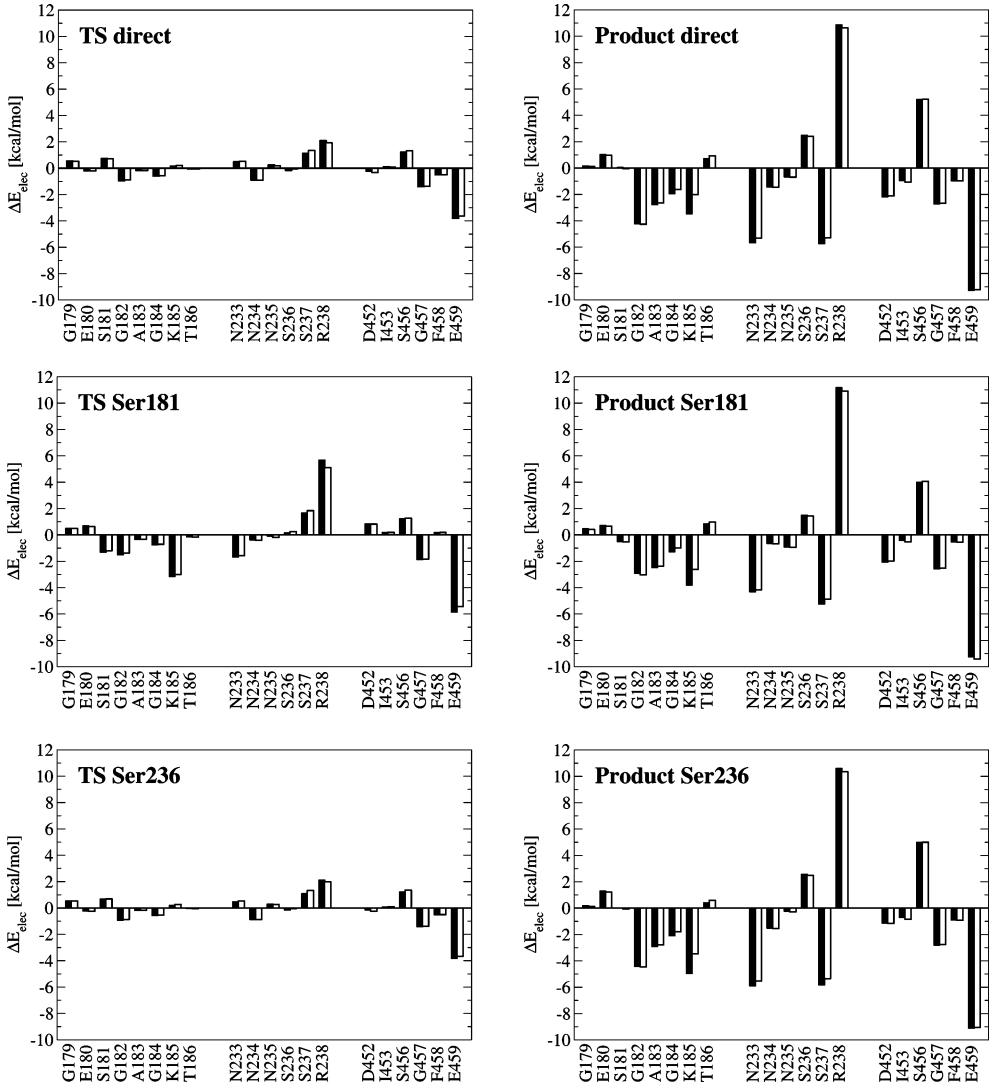


FIGURE 7: Electrostatic energy contributions to the barrier heights and reaction energies from individual residues of the P-loop (residues 179−186), the Switch-1 loop (residues 233−238), and the Switch-2 loop (residues 452−459), defined as $\Delta E^{X}_{elec}$ in Methods. For the residues included in the QM region (i.e., Ser181, Thr186, Ser237, and Ser237), only the effects of the charges on the backbone atoms are considered. Black bars: HF/6-31G(d,p). White bars: B3LYP/6-31+G(d,p)//HF/6-31G(d,p).

Switch-2 loops and has been shown to be essential for hydrolysis of ATP by myosin (*78*). In all three paths, interactions with Glu459 lower the barrier (by approximately −4 kcal/mol in the direct and Ser236 paths and approximately −6 kcal/mol in the Ser181 path), whereas interactions with Arg238 raise the barrier by a similar amount (by approximately 2 kcal/mol in the direct and Ser236 paths and approximately 6 kcal/mol in the Ser181 path). Thus, the contribution of Arg238 offsets, at least partially, the favorable contribution of Glu459, and the total contribution of the salt bridge residues to the barrier height is negligible. This indicates that the likely role of this essential salt bridge is to lock in the active site, rather than to participate directly in the catalysis. Gly457, which hydrogen bonds to the $\gamma$-phosphate, lowers the barrier in all three paths by approximately 2 kcal/mol. The remaining residues do not contribute significantly to the lowering of the barrier.

The residue contributions to the net change in energy after the reaction are also shown in Figure 7 (right panels). Not surprisingly, the contributions are similar for all three paths, given the similarity of their product states. As in the transition states, the unfavorable contribution of Arg238 (~11 kcal/mol) offsets the favorable contribution of Glu459 (approximately −9 kcal/mol) such that the total contribution of the Arg238−Glu459 salt bridge to the reaction energy is again small. Large favorable contributions are observed for Asn233 (from −4 to −6 kcal/mol), the backbone atoms of Ser237 (approximately −6 kcal/mol), and Lys185 (approximately −9 kcal/mol). Few residues exhibit unfavorable contributions to the reaction energy, except for Ser456 (4−5 kcal/mol). The total contribution of all binding-pocket-forming residues (the residues listed in Figure 7) to the reaction energy amounts to −21.7 (−19.1) kcal/mol, −18.4 (−16.7) kcal/mol, and −22.5 (−20.2) kcal/mol with HF (B3LYP) for the product states of the direct, Ser181, and Ser236 paths, respectively. These values include the combined MM and QM/MM electrostatic contributions of the residues of the binding pocket but are dominated by the QM/MM electrostatics. The binding-pocket-forming residues contribute approximately half of the total QM/MM electrostatic stabilization energy that stabilizes the anionic charge pair ($P_i^-$ and $ADP^{3-}$) in the product state.

Table 4: Charge Transfers during the Reaction

| | | $\Delta\sum q$(transition state)[b] | | |
|---|---|---|---|---|
| moiety | $\sum q$(reactant)[a] | direct | Ser181 | Ser236 |
| $H_2O^h$ | −0.05 (0.03) | 0.00 (−0.01) | 0.02 (−0.03) | 0.00 (−0.01) |
| Ser181 | −0.02 (−0.02) | 0.02 (0.01) | −0.01 (0.03) | 0.02 (0.01) |
| Ser236 | −0.02 (−0.06) | −0.04 (−0.01) | −0.05 (0.02) | −0.04 (−0.01) |
| $H_2O^a$ | −0.01 (0.07) | −0.27 (−0.37) | −0.29 (−0.44) | −0.27 (−0.37) |
| ATP | −3.37 (−3.07) | 0.32 (0.47) | 0.34 (0.50) | 0.32 (0.46) |
| ATP·$H_2O^a$ | −3.38 (−3.00) | 0.04 (0.10) | 0.06 (0.05) | 0.04 (0.10) |
| ADP[c] | −2.29 (−2.32) | −0.04 (−0.05) | −0.04 (−0.07) | −0.04 (−0.05) |
| $P_i$[c] | −1.09 (−0.68) | 0.08 (0.14) | 0.10 (0.13) | 0.08 (0.14) |
| $Mg^{2+}$ | 1.20 (0.21) | −0.03 (−0.11) | −0.02 (−0.06) | −0.03 (−0.10) |
| Ser237 | 0.05 (0.18) | 0.00 (0.01) | 0.00 (0.01) | 0.00 (0.01) |
| Thr186 | 0.06 (0.29) | −0.01 (−0.02) | −0.01 (−0.03) | −0.01 (−0.02) |
| $H_2O^{w1}$ | 0.09 (0.21) | 0.01 (0.00) | 0.00 (0.00) | 0.01 (0.00) |
| $H_2O^{w2}$ | 0.07 (0.16) | 0.01 (0.02) | 0.00 (0.01) | 0.01 (0.02) |

| | $\Delta\sum q$(product state)[b] | | |
|---|---|---|---|
| moiety | direct | Ser181 | Ser236 |
| $H_2O^h$ | 0.04 (0.00) | 0.05 (−0.04) | 0.04 (0.00) |
| Ser181 | 0.03 (0.05) | −0.02 (0.04) | 0.03 (0.05) |
| Ser236 | 0.01 (0.04) | 0.03 (0.04) | 0.02 (0.04) |
| $H_2O^a$[d] | 0.03 (−0.09) | 0.12 (−0.04) | 0.03 (−0.11) |
| ATP[d] | 0.00 (0.20) | −0.10 (0.12) | −0.01 (0.19) |
| ATP·$H_2O^a$[d] | 0.03 (0.11) | 0.02 (0.08) | 0.02 (0.08) |
| ADP | −0.27 (0.02) | −0.26 (0.01) | −0.28 (0.01) |
| $P_i$ | 0.31 (0.08) | 0.28 (0.07) | 0.30 (0.08) |
| $Mg^{2+}$ | −0.06 (0.03) | −0.04 (0.06) | −0.05 (0.05) |
| Ser237 | −0.07 (−0.15) | −0.06 (−0.14) | −0.06 (−0.15) |
| Thr186 | 0.01 (−0.05) | 0.01 (−0.02) | 0.00 (−0.06) |
| $H_2O^{w1}$ | −0.01 (−0.02) | −0.01 (−0.02) | 0.00 (−0.01) |
| $H_2O^{w2}$ | 0.01 (0.00) | 0.01 (0.01) | 0.01 (0.00) |

[a] The atomic Mulliken charges are summed for different moieties in the reactant state, $\sum_{\text{moiety}} q$. [b] Differences in sums ($\Delta\sum_{\text{moiety}} q$) between the transition and reactant state (top half) or between the product and reactant state (bottom half) of the different paths optimized with HF/6-31G(d,p) are based on single-point energy calls using HF/6-31G(d,p) or B3LYP/6-31+G(d,p) (numbers in parentheses). Proton charges are counted toward the heavy atoms to which they are bound in the different states. [c] All atoms in the reactant or the transition states that will form the ADP or $P_i$ in the product state. [d] All atoms in the product state that had formed the ATP or attacking water ($H_2O^a$) in the reactant state.

### *Charge Transfer*

Table 4 summarizes the partial charges on the different moieties included in the QM region as determined for the stationary points of the three paths. In the reactant state, the Mulliken charge on the $Mg^{2+}$ cation is only 1.20*e* with HF/6-31G(d,p) [0.21*e* with B3LYP/6-31+G(d,p)], while the four $Mg^{2+}$-coordinating groups (two water molecules and the side chains of Thr186 and Ser237) carry a fractional positive charge. This indicates that the positive $Mg^{2+}$ partially possesses the electrons of these coordinating groups.

Likewise, the total Mulliken charge on the triphosphate moiety of $ATP^{4-}$ is −3.37*e* with HF/6-31G(d,p) [−3.07*e* with B3LYP/6-31+G(d,p)], less negative than its formal charge of −4, indicating that a significant amount of negative charge is transferred from $ATP^{4-}$ to $Mg^{2+}$. In contrast, the ADP moiety of ATP carries a charge of −2.29*e* (−2.32*e*) and is thus more negative than its formal charge of −2. Thus, most of the electrons pulled toward the $Mg^{2+}$ come from the $P_\gamma$ group of ATP, preparing it for attack by a nucleophile. The attacking water molecule is essentially neutral (−0.01*e* and 0.07*e*), as is the helper water molecule (−0.05*e* and 0.03*e*). In the reactant, the sum of Mulliken charges on the attacking water and the $\gamma$-phosphate atoms (i.e., all atoms that form the inorganic phosphate in the product state) is −1.09*e* (−0.68*e* with B3LYP). This is essentially what is expected for an $H_2PO_4^-$ group, as opposed to the expected formal charge of −2 on the $\gamma$-phosphate moiety of ATP. Thus, the electrostatic charge distribution of the product state is already preformed in the reactant state. This is the reason the Mulliken charges on these moieties are essentially the same in the transition state and in the reactant state ($\Delta\sum q$, Table 4).

Noticeable charge shifts occur for only the moieties that are directly involved in the hydrolysis. The changes between the transition and the reactant states can be traced back to a small number of atomic charge shifts. The attacking water $H_2O^a$ loses a proton upon formation of the transition state, thus increasing the charge accumulated on the oxygen. In the TS, the $O^a$ carries a charge of approximately −1*e* compared to a charge of approximately −0.75*e* in the reactant or product states. This leads to the observed charge shifts on $H_2O^a$. The fractional charge accumulated on $O^a$ in the TS originates from $P_\gamma$ and $O_{\gamma 2}$, both of which are noticeably more positive in the TS than in the reactant. Consequently, the total charge on ATP is more positive in the TS than in the reactant, whereas the sum of charges on ATP·$H_2O^a$ remains constant. Since this charge redistribution mainly involves atoms that will form the $P_i$ in the product state, neither the $P_i$ nor the ADP moieties exhibit marked charge differences between the transition and the reactant states.

Charge shifts on moieties between the product and the reactant states are observed only for the Hartree−Fock Mulliken analysis and not for the B3LYP results. Unlike in the case of the TS, these charge shifts cannot be traced back to changes in the Mulliken charges of specific atoms. Rather, they are the result of cumulative effects of small atomic charge changes that occur on all atoms and that happen to add up with HF but cancel out with B3LYP. Thus, the charge shifts observed with HF are not meaningful, and no significant charge shifts occur between the reactant and product states.

## DISCUSSION

*Associative versus Dissociative Mechanism.* Experiments used to determine linear free energy relationships for a number of uncatalyzed phosphoanhydride hydrolysis reactions show only a small dependence of the hydrolysis rate constant on the p$K_a$ of different incoming groups but a large dependence on the p$K_a$ of leaving groups (*14*). This was interpreted in favor of a dissociative mechanism in aqueous solution in ref *14*. However, the unique interpretability of linear free energy relationships is questionable (*79*). Moreover, hydrolysis in aqueous solution of methyl phosphate, the smallest possible model system for phosphate hydrolysis, which has been examined using a variety of methods, can be explained using either associative or dissociative mechanisms (*77*, *80*−*82*), and computational investigations on methyl triphosphate hydrolysis in aqueous solution also did not give clear evidence in favor of either mechanism (*75*, *77*). Since neither mechanism seems to be inherently more favorable, enzymes can, in principle, select either (*83*, *84*).

In all three mechanisms for water activation investigated here, ATP hydrolysis is found to follow an associative route, via a pentacovalent transition state. This agrees well with the findings from reaction quenching experiments that ruled

out a detectable metaphosphate intermediate and, therefore, an unambiguous dissociative mechanism (*23*), oxygen exchange experiments that suggest a single-step mechanism (*22*), and Raman spectroscopy that indicated a transition state with associative character (*27*). Also, a previous QM/MM study on ATP hydrolysis in myosin yielded an associative route (*35*). However, in ref *35*, the pentacovalent structure was found to be stable (i.e., a local minimum along the reaction profile). Although that study used reaction path refinements with the CPR algorithm in combination with Hartree−Fock QM/MM, as were used here, the calculations in ref *35* differed from those presented here in the crystal structure, the QM basis sets, and the treatment of solvent electrostatic screening effects during path refinement. First, in our study, a structure with Be•$F_x$•ADP, i.e., an ATP analogue, was used to model the ATP-bound reactant state, whereas in ref *35*, the calculations started from a $VO_4$•ADP structure, i.e., a transition-state analogue. Second, nonuniform charge scaling is applied here to account for the solvent screening effect on each protein partial charge, whereas in ref *35*, only the solvent-exposed ionized side chains were scaled. Finally, the previous study used the 3-21+G basis set, whereas our study employs a 6-31G(d,p) basis set, which encompasses more basis functions and yields more reliable structural results (see Results).

*Water Activation.* At every level of theory used here, the three water activation mechanisms have approximately the same barriers and are thus approximately equally likely. This suggests that myosin maintains a preorganized, dynamic hydrogen bonding network in the active site when it adopts the catalytically competent C/C conformation. This dynamical network consists of the $\gamma$-phosphate, water molecules adjacent to the $\gamma$-phosphate, and side chains that can carry protons and serve as proton donors and/or acceptors. The central core of the network is formed by the water molecules which are trapped in the proximity of the $\gamma$-phosphate moiety of ATP when myosin adopts its prehydrolysis conformation. Because of the rotational freedom of the water molecules and their capacity to both donate and accept a proton in different directions, they serve as ideal proton shuttles, mediating proton transfers between the key amino acids.

In the results presented here, the side chains of Ser181 and Ser236 also participate in the proton transfer events. The protons can rapidly exchange between the donor and acceptor groups via pathways with low energy barriers (relative to the hydrolysis barrier), in a fashion similar to the transport of hydrated hydroxide in aqueous solution, for which the free energy of activation has been estimated to be 3 kcal/mol (*76*). For several such hydrogen bonding patterns, ATP hydrolysis proceeds with the same movements of the heavy atoms, in particular, the movement of $P_\gamma$ and $Mg^{2+}$. In principle, more paths in addition to those studied here are conceivable with different protonation patterns of the myosin active site, for example, involving the participation of the side chains of Lys185, Arg238, Ser456, or Glu459 in the dynamic hydrogen bonding network. In such a scenario, the reaction mechanisms suggested prior to this work (*28*−*32*) would correspond to water activation mechanisms that occur via different proton transfer routes, starting from different protonation patterns of the myosin active site.

*Role of Central Residues.* Ser181 and Ser236 both participate in the postulated dynamic hydrogen bonding network. Mutating either into Ala would therefore be expected to reduce the number of possible proton transfer routes for water activation, thus leading to reduced, but not abolished, ATPase activity. This is indeed observed, for both Ser181 (*33*) and Ser236 (*33*, *34*). Thus, the role of these residues may be to facilitate the proton relays required for hydrolysis. It would be interesting to measure the ATPase activity for the Ser181/Ser236 double mutant, the activity level of which would give information about the relative importance of the direct activation mechanism. Measurements of the basal ATPase activity (i.e., the combined rate from substrate binding, hydrolysis, and product release steps) of a number of myosin mutants have been reported (*33*, *34*, *78*, *85*, *86*). The effect of mutations on the rate of the hydrolysis step itself (step 3b) cannot be derived directly from the measurement of the basal ATPase rate but require experiments that have been described for the W501+ construct (which were used to construct the free energy profile of the ATPase cycle shown in Figure 1). To our knowledge, such measurements have not been reported.

It had been assumed that, when a mutation affecting the basal ATPase rate is located in the immediate neighborhood to the ATP binding site, its effect on the ATPase rate stems from an influence on the ATP hydrolysis step. These calculations show, however, that this is not true for all residues under consideration. When salt bridge residues Arg238 and Glu459 are mutated such that salt bridge formation is made impossible, ATPase activity is lost [e.g., R238A (*34*), R238C (*34*), R238H (*34*), R238I (*33*), R238E (*78*), E459A (*85*), E459V (*86*), and E459R (*78*)], but the results presented here have shown that the interactions of ATP with these two residues do not significantly modify the reaction barrier of ATP hydrolysis. Indeed, in mutants that can form a different salt bridge [i.e., R238K (*33*) and the double mutant R238E/E459R (*78*)], ATPase activity is preserved. Thus, the role of the salt bridge is to form the active site pocket and to sequester a small number of water molecules in the reactive area (e.g., the attacking water and the helper water). Arg238 and Glu459 do not seem to have a direct catalytic effect, in the sense that the salt bridge as a whole does not lower the activation barrier.

Gly457 is found here to slightly stabilize the transition state. This stabilization is, however, not so pronounced that it allows assignment of a clear catalytic role to Gly457 in lowering the reaction barrier. This residue may, however, be involved in destabilizing the ground state by forming a hydrogen bond to the $\gamma$-phosphate, which could explain why the ATPase activity is significantly reduced when Gly457 is mutated to Ala (*85*). It has also been suggested that Gly457 is a key residue involved in coupling the activation of the ATP hydrolysis function to the priming of the lever arm during the recovery stroke (*12*).

*Role of $Mg^{2+}$.* The formation of the coordination bonds between $Mg^{2+}$ and $ATP^{4-}$ introduces an asymmetry in the $\{P_\gamma-O_{\beta\gamma}\}$ and $\{O_{\beta\gamma}-P_\beta\}$ distances. An equivalent asymmetry had been observed for $Mg^{2+}$•methyl triphosphate in solution (*75*). Even in pyrophosphate, a symmetric molecule, an asymmetry between the two $\{P-O_{bridge}\}$ bonds is introduced in the gas phase by complexation with $Mg^{2+}$ when the $Mg^{2+}$ is coordinated by one oxygen of one phosphate moiety and two oxygens of the other phosphate moiety (*87*). This asymmetry of the $\{P-O_{bridge}\}$ bond lengths in all these

cases indicates that $Mg^{2+}$ in myosin is placed in such a way that it activates the $\{P_\gamma-O_{\beta\gamma}\}$ bond for cleavage.

In the product states described here, the $Mg^{2+}$ cation moves somewhat between the $ADP^{3-}$ and $P_i^-$ moieties upon decay of the pentacovalent oxyphosphorane transition state (see the movies), thereby helping in electrostatic stabilization of the highly repulsive anion pair as well as sterically separating the reaction products. This contributes to the lowering of the energy of the product state. According to the Hammond postulate, stabilization of the product state shifts the transition state toward the reactant state (*88*). Indeed, the transition state is seen here to be structurally and electrostatically close to the reactant state. Given that the energy of the unhydrolyzed ATP is much lower than that of the anion pair in its proximity, this is one way for the protein to lower the activation barrier.

*Enzymatic Strategy of Myosin.* In lowering the barrier of ATP hydrolysis from 28.9 to 29.3 kcal/mol (*13*, *14*) in aqueous solution to ~14.5 kcal/mol in the myosin active site, myosin functions as an enzyme. Enzymes can, in principle, achieve catalysis by destabilizing the reactant state and/or stabilizing the rate-limiting transition state. In this work, we find that the residues in the direct proximity of the reaction do not significantly contribute to lowering the barrier. Therefore, no clear stabilization of the transition state is observed. In contrast, factors that may contribute to reactant-state destabilization are indeed observed. These factors are the preformation of the charge pattern of the transition state in the reactant state and the deformation of ATP toward the trigonal bipyramidal transition-state geometry, as well as the asymmetry of the $\{P-O_{\beta\gamma}\}$ bonds. Thus, myosin is likely to act mainly by destabilization of the reactant state.

This destabilization effect is difficult to quantify in this case. It requires a comparison of (1) the energy of isolated ATP taken in the conformation it has when bound to myosin, including electronic effects the protein exerts on ATP, and (2) the energy of unbound ATP in aqueous solution. The latter is, however, difficult to compute. In aqueous solution and in the presence of $Mg^{2+}$, ATP exists in a number of different protonation states, such as $Mg{\cdot}H_2ATP$ or $Mg{\cdot}HATP^-$. The properties of these species and the equilibria between them are well-known (*89*). However, each species exists in an ensemble of "subspecies". For example, neutral $Mg{\cdot}H_2ATP$ can have the two hydrogens distributed over the seven terminal oxygens of the triphosphate moiety in several ways, and for each such distribution, $Mg{\cdot}H_2ATP$ can adopt a number of conformations that need to be sampled. The energies of all resulting microstates must be averaged to derive the free energy of that species. Each microstate undergoes a different destabilization upon binding, with different contributions from effects such as geometric deformation, electronic polarization and charge transfer, and changes in protonation. Because each of these binding effects would have to be determined for each unbound ATP microstate, this considerably complicates the quantification of the destabilization energy.

*Chemomechanical Coupling.* The breaking of the coordination bond between $Mg^{2+}$ and Ser237 (see the movies) implies that the Switch-1 loop is no longer immobilized by this strong interaction. Just as formation of this coordination bond accompanies the closure of the Switch-1 loop upon ATP binding, breaking of this bond can be considered a prerequisite for the opening of the Switch-1 loop after hydrolysis. Since motion of the Switch-1 loop is believed to be coupled to cleft closure (*90*, *91*), and thereby modulation of the actin affinity (*92*, *93*), weakening of the $Mg^{2+}$–Switch-1 interaction as observed here is a key event that couples the hydrolysis step to the conformational changes of the posthydrolytic events of the actomyosin cycle. Such a coupling might occur via a cooperative mechanism, in which small movements of Switch-1 would facilitate the partial cleft closure that induces initial actin binding (the so-called "weak binding" state of actomyosin), the strengthening of which induces a further cleft closing that propagates back to the Switch-1 loop, which fully opens to allow the release of $P_i$ (*94*; compare Figure 1 therein). The present simulations strengthen the hypothesis that, in the actomyosin contractile cycle, the hydrolysis products are released via an exit route that opens by movement of Switch-1, in a mechanism that has been termed a "trap door" (*95*), rather than along an exit route in which $P_i$ is released into the 50 kDa cleft by breaking of the Arg238–Glu459 salt bridge (the "back door" mechanism) (*96*).

To ensure efficacy in force production by myosin, it is necessary to prevent premature and thus ineffective product release. This makes it necessary to keep $P_i$ and ADP bound after hydrolysis has occurred until structural rearrangements in the myosin motor have prepared the system for the power stroke. Since both $P_i$ and ADP carry large negative charges and thus strongly repel each other, it is difficult to keep them both bound in the active site of myosin where they are in very close contact with each other. The present results show that this task is achieved in myosin by the strong stabilization of the product state by means of the electrostatic interactions with the surrounding protein that are more favorable in the product state than in the reactant state (Figure 6C,D). Half of this stabilization energy can be assigned to the residues in direct contact with ATP (Figure 7). However, the contribution of longer-range electrostatic interactions to stabilization of the product state cannot be neglected. Further analysis is required to gain detailed insight into the mechanism that eventually allows the products to be released upon actin binding.

*Oxygen Exchange.* Isotope exchange experiments aimed at investigating ATP hydrolysis in myosin have established that all four oxygens on the product $P_i$ can equivalently exchange with the bulk solvent (solvent–phosphate exchange) (*21*), whereas the $\beta\gamma$-bridge oxygen and the $\beta$-oxygens do not exchange (positional isotope exchange) (*19*). This exchange of the terminal $\gamma$-oxygens requires that the $P_i$ in the product state possesses rotational freedom. In the posthydrolysis state of this simulation, the $\{Mg^{2+}-O^{S237}\}$ coordination bond is broken and $Mg^{2+}$ is only 5-fold coordinated after hydrolysis. Moreover, the $\{Mg^{2+}-O_{\gamma3}\}$ coordination bond is longer and thus weaker than the $\{Mg^{2+}-O_{\beta2}\}$ bond (see Table 3), indicating that in the posthydrolysis state the former is more likely to break than the latter. This makes it possible for the $P_i$ to transiently dissociate from $Mg^{2+}$, yielding a 4-fold coordinated $Mg^{2+}$ cation and allowing the $P_i$ to rotate. In such a scenario, the $\beta$-phosphate remains permanently coordinated to $Mg^{2+}$, hindering its rotation, which explains the experimentally observed lack of positional isotope exchange. Thus, the product structure found here, with its 5-fold $Mg^{2+}$ coordina-

tion and weakened $\{Mg^{2+}-O_{\gamma 3}\}$ bond, is consistent with the experimentally observed features of the oxygen exchange. Moreover, breaking of the $\{Mg-O_{\gamma 3}\}$ bond as proposed here must eventually occur to allow exit of the $P_i$. The description mentioned above gives a possible scenario of this crucial event early after hydrolysis.

Five- or four-coordinated $Mg^{2+}$ complexes are not unusual, as they are observed in ~10 and 23% of Mg-containing structures in the Cambridge Crystallographic Databank, compared to 60% with a coordination number of six (*97*). The hypothesis that intermediary 4-fold metal coordination is required is supported by measurements of intermediate solvent−phosphate isotope exchange in the presence of a number of divalent cations (*98*). No exchange is observed with $Ca^{2+}$, $Sr^{2+}$, or $Ba^{2+}$, none of which allow for a coordination number of four (*97*), and thus for intermediate dissociation of the metal−$P_i$ coordination bond. In contrast, exchange is observed in the presence of $Co^{2+}$, $Ni^{2+}$, or $Mn^{2+}$, each of which allows coordination numbers of six and four (*97*).

Direct evidence of the existence of a tetracoordinate metal intermediate in the myosin ATPase cycle might be obtained from time-resolved EPR spectroscopy using $Mn^{2+}$ as a metal cofactor. When a $^{17}O$ directly coordinates to $Mn^{2+}$, the EPR signal for $Mn^{2+}$ is inhomogeneously broadened. This has been used to investigate the myosin·Mn·ADP complex (*99*). When ATP with all terminal $\gamma$-oxygens labeled with $^{17}O$ was used, a broadening of the EPR signal should be observed as long as a terminal $\gamma$-oxygen coordinates to $Mn^{2+}$. If the hypothesis holds that the $P_i$−metal coordination bond breaks and reforms during the reversible hydrolysis, then an oscillatory signal broadening should be observable in time-resolved EPR experiments in the initial phase of the experiment before solvent−phosphate isotope exchange occurs.

*Validity and Accuracy.* The question of the reliability of the simulation results arises. That the simulations have successfully reproduced the qualitative nature of ATP hydrolysis in myosin is shown by comparison with experiment. (1) Hydrolysis was found to proceed in a single step, consistent with experiment (*22*). (2) The associative nature of the transition state is consistent with the observed inversion of configuration (*24*). (3) The simulation-based hypothesis that $Mg^{2+}$ adopts a coordination number of four is consistent with findings from experimental studies in which isotope exchange effects were investigated (*19*).

The main conclusions of the work are drawn from structural considerations that can safely be made because it was shown that the structures optimized with HF/6-31G-(d,p) have converged. Reliable and interpretable energies, however, are much more difficult to obtain. At this level of theory, the absolute values of the barrier height and reaction energy still depend on the quantum method and basis set. Nevertheless, the calculations reported here represent the most accurate calculations on enzyme-catalyzed nucleoside triphosphate hydrolysis to date. Higher-level quantum methods could not be employed due to computational limitations [optimization of one path takes 2−4 months on eight CPUs at 2.6 GHz with HF/6-31G(d,p)]. Although the absolute energies are thus unreliable, an identical systematic error can be expected for a given quantum method, given basis set, and unchanging atomic constitution of the QM region, which makes it possible to compare the three different paths investigated relative to each other. With regard to previous QM/MM studies on nucleoside triphosphate hydrolysis that used a 3-21+G basis set, a mixed 4-31G(d) and 3-21G basis set, or a 6-31G(d) basis set during geometry optimizations to study ATP hydrolysis in myosin (*35*), GTP hydrolysis in Ras-GAP (*100*), or ATP hydrolysis in $F_1$-ATPase (*101*, *102*), it should be noted that we show here that the 3-21G(d) basis set is not sufficient even for obtaining reliable geometries.

All the calculated potential energy barriers are significantly higher than the ~14.5 kcal/mol experimental free energy barrier. In addition to the errors inherent to the level of the quantum method used, there may be other contributions to the deviation between experimental and calculated energy barriers. First, the protein conformation in the crystal structure may not be in the geometry that is optimal for the hydrolysis event. Even though the crystal structure used in this study was determined with the ATP analogue ADP·Be·$F_3$ bound to myosin in the C/C conformation (*47*), it is possible that some side chains are in conformations that are not yet optimal for hydrolysis. Second, the experimentally determined reaction barrier is a free energy barrier, unlike the potential energy barriers derived from the present minimum energy paths. However, to allow free energy calculations, fast semiempirical methods would have to be used. These calculations are not possible at present, since validated parameters for phosphate−anhydride hydrolysis reactions are not currently available for the semiempirical AM1/d (*103*−*105*), MNDO/d (*106*, *107*), or SCC-DFTB (*108*) methods, which otherwise might be suitable for this purpose.

## CONCLUSION

In this study, three different water activation mechanisms for ATP hydrolysis in myosin were investigated with theoretical methods. Hydrolysis was found to proceed in a single-step reaction in the three corresponding reaction paths via an associative route. In the product state, the coordination bond between the $Mg^{2+}$ metal cofactor and Ser237 in the Switch-1 loop is broken, thereby facilitating the opening of the Switch-1 loop after hydrolysis is completed. This is likely to be the key element for the chemomechanical coupling between ATP hydrolysis and subsequent actin binding in the motor cycle. Moreover, by proposing the presence of a dynamic hydrogen bonding network leading to a variety of possible reaction routes that the system can take, this work gives a new perspective on the hydrolysis mechanism in myosin.

Structural conditions similar to those present in the active site of myosin are also found in the motor protein $F_1$-ATPase (*101*, *102*) and, judging from available crystal structures, seem also to be possible in the GTPase of the Ras family of signaling proteins (*109*, *110*). In these proteins, water activation during nucleoside triphosphate hydrolysis may proceed via a hydrogen bonding network similar to the one outlined here for myosin. Whether early posthydrolytical chemomechanical coupling mechanisms similar to that found here for myosin occur in other motor proteins remains to be investigated.

## ACKNOWLEDGMENT

We thank Ken Holmes and Clive Bagshaw for helpful discussions.

## REFERENCES

1. Bloom, G. S. (2000) Preface, *Biochim. Biophys. Acta 1496*, 1−2.
2. Sellers, J. R. (2000) Myosins: A diverse superfamily, *Biochim. Biophys. Acta 1496*, 3−22.
3. Berg, J. S., Powell, B. C., and Cheney, R. E. (2001) A millennial myosin census, *Mol. Biol. Cell 12*, 780−794.
4. Kull, F. J., Sablin, E. P., Lau, R., Fletterick, R. J., and Vale, R. D. (1996) Crystal structure of the kinesin motor domain reveals a structural similarity to myosin, *Nature 380*, 550−559.
5. Vale, R. D. (1996) Switches, latches, and amplifiers: Common themes of G proteins and molecular motors, *J. Cell Biol. 135*, 291−302.
6. Smith, C. A., and Rayment, I. (1996) Active site comparisons highlight structural similarities between myosin and other P-loop proteins, *Biophys. J. 70*, 1590−1602.
7. Kull, F. J., Vale, R. D., and Fletterick, R. J. (1998) The case for a common ancestor: Kinesin and myosin motor proteins and G proteins, *J. Muscle Res. Cell Motil. 19*, 877−886.
8. Holmes, K. C., and Geeves, M. A. (2000) The structural basis of muscle contraction, *Philos. Trans. R. Soc. London, Ser. B 355*, 419−431.
9. Geeves, M. A., and Holmes, K. C. (1999) Structural mechanism of muscle contraction, *Annu. Rev. Biochem. 68*, 687−728.
10. Geeves, M. A., and Holmes, K. C. (2005) The molecular mechanism of muscle contraction, *Adv. Protein Chem. 71*, 161−193.
11. Itakura, S., Yamakawa, H., Toyoshima, Y. Y., Ishijima, A., Kojima, T., Harada, Y., Yanagida, T., Wakabayashi, T., and Sutoh, K. (1993) Force-generating domain of myosin motor, *Biochem. Biophys. Res. Commun. 196*, 1504−1510.
12. Fischer, S., Windshügel, B., Horak, D., Holmes, K. C., and Smith, J. C. (2005) Structural mechanism of the recovery stroke in the myosin molecular motor, *Proc. Natl. Acad. Sci. U.S.A. 102*, 6873−6878.
13. Miller, D. L., and Westheimer, F. H. (1966) The hydrolysis of $\gamma$-phenylpropyl di- and triphosphates, *J. Am. Chem. Soc. 88*, 1507−1511.
14. Admiraal, S. J., and Herschlag, D. (1995) Mapping the transition state for ATP hydrolysis: Implications for enzymatic catalysis, *Chem. Biol. 2*, 729−739.
15. Cope, M. J. T. V., Whisstock, J., Rayment, I., and Kendrick-Jones, J. (1996) Conservation within the myosin motor domain: Implications for structure and function, *Structure 4*, 969−987.
16. Webb, M. R., and Trentham, D. R. (1983) Chemical mechanism of myosin-catalyzed ATP hydrolysis, in *Handbook of physiology: skeletal muscle* (Peachey, L. D., Adrian, R. H., and Geiger, S., Eds.) pp 237−255, American Physiological Society, Bethesda, MD.
17. Dempsey, M. E., Boyer, P. D., and Benson, E. S. (1963) Characteristics of an orthophosphate oxygen exchange catalysed by myosin, actomyosin, and muscle fibers, *J. Biol. Chem. 238*, 2708−2715.
18. Swanson, J. R., and Yount, R. (1966) The properties of heavy meromyosin and myosin catalyzed medium and intermediate $^{18}$O-phosphate exchange, *Biochem. Z. 345*, 395−409.
19. Dale, M. P., and Hackney, D. D. (1987) Analysis of positional isotope exchange in ATP by cleavage of the $\beta$P−O$\gamma$P bond. demonstration of negligible positional isotope exchange by myosin, *Biochemistry 26*, 8365−8372.
20. Bagshaw, C. R., Trentham, D. R., Wolcott, R. G., and Boyer, P. D. (1975) Oxygen exchange in the $\gamma$-phosphoryl group of protein-bound ATP during $Mg^{2+}$-dependent adenosine triphosphatase activity of myosin, *Biochemistry (Moscow) 72*, 2592−2596.
21. Sleep, J. A., Hackney, D. D., and Boyer, P. D. (1980) The equivalence of phosphate oxygens for exchange and the hydrolysis characteristics revealed by the distribution of [$^{18}$O]$P_i$ species formed by myosin and actomyosin ATPase, *J. Biol. Chem. 255*, 4094−4099.
22. Webb, M. R., and Trentham, D. R. (1981) The mechanism of ATP hydrolysis catalysed by myosin and actomyosin, using rapid reaction techniques to study oxygen exchange, *J. Biol. Chem. 256*, 10910−10916.
23. Sartorelli, L., Fromm, H. J., Benson, R. W., and Boyer, P. D. (1966) Direct and $^{18}$O-exchange measurements relevant to possible activated or phosphorylated states of myosin, *Biochemistry 5*, 2877−2884.
24. Webb, M. R., and Trentham, D. R. (1980) The stereochemical course of phosphoric residue transfer during the myosin ATPase reaction, *Biochem. J. 255*, 8629−8632.
25. Young, J. H., McLick, J., and Korman, E. F. (1974) Pseudorotation mechanism of ATP hydrolysis in muscle contraction, *Nature 249*, 474−476.
26. López, C. S., Faza, O. N., de Lera, A. R., and York, D. M. (2005) Pseudorotation barriers of biological oxyphosphoranes: A challenge for simulations of ribozyme catalysis, *Chem.—Eur. J. 11*, 2081−2093.
27. Deng, H., Wang, J., Callender, R. H., Grammer, J. C., and Yount, R. G. (1998) Raman difference spectroscopic studies of the myosin S1·MgADP·vanadate complex, *Biochemistry 37*, 10972−10979.
28. Fisher, A. J., Smith, C. A., Thoden, J., Smith, R., Sutoh, K., Holden, H. M., and Rayment, I. (1995) X-ray structures of the myosin motor domain of *Dictyostelium discoideum* complexed with MgADP·$BeF_x$ and MgADP·$AlF_4^-$, *Biochemistry 34*, 8960−8972.
29. Rayment, I. (1996) The structural basis of the myosin ATPase activity, *J. Biol. Chem. 271*, 15850−15853.
30. Kagawa, H., and Mori, K. (1999) Molecular orbital study of the interaction between MgATP and the myosin motor domain: The highest occupied molecular orbitals indicate the reaction site of ATP hydrolysis, *J. Phys. Chem. B 103*, 7346−7352.
31. Minehardt, T. J., Marzari, N., Cooke, R., Pate, E., Kollmann, P. A., and Car, R. (2002) A classical an ab initio study of the interaction of the myosin triphosphate binding domain with ATP, *Biophys. J. 82*, 660−675.
32. Onishi, H., Mochizuki, N., and Morales, M. F. (2004) On the myosin catalysis of ATP hydrolysis, *Biochemistry 43*, 3757−3763.
33. Li, X., Rhodes, T. E., Ikebe, R., Kambara, T., White, H. D., and Ikebe, M. (1998) Effects of mutations in the $\gamma$-phosphate binding site of myosin on its motor function, *J. Biol. Chem. 273*, 27404−27411.
34. Shimada, T., Sasaki, N., Ohkura, R., and Sutoh, K. (1997) Alanine scanning mutagenesis of the switch I region in the ATPase site of *Dictyostelium discodeum* myosin II, *Biochemistry 36*, 14037−14043.
35. Li, G., and Cui, Q. (2004) Mechanochemical coupling in myosin: A theoretical analysis with molecular dynamics and combined QM/MM reaction path calculations, *J. Phys. Chem. B 108*, 3342−3357.
36. Okimoto, N., Yamanaka, K., Ueno, J., Hata, M., Hoshino, T., and Tsuda, M. (2001) Theoretical studies on the ATP hydrolysis mechanism of myosin, *Biophys. J. 81*, 2786−2794.
37. Málnási-Csizmadia, A., Woolley, R. J., and Bagshaw, C. R. (2000) Resolution of conformational states of *Dictyostelium* myosin II motor domain using tryptophan (W501) mutants: Implications for the open-closed transition identified by crystallography, *Biochemistry 39*, 16135−16146.
38. Simmons, R. M., and Hill, T. L. (1976) Definition of free energy levels in biochemical reactions, *Nature 263*, 615−618.
39. Málnási-Csizmadia, A., Pearson, D. S., Kovács, M., Woolley, R. J., Geeves, M., and Bagshaw, C. R. (2001) Kinetic resolution of a conformation transition and the ATP hydrolysis step using relaxation methods with a *Dictyostelium* myosin II mutant containing a single tryptophan residue, *Biochemistry 40*, 12727−12737.
40. Zeng, W., Conibear, P. B., Dickens, J. L., Cowie, R. A., Wakelin, S., Málnási-Csizmadia, A., and Bagshaw, C. R. (2004) Dynamics of actomyosin interactions in relation to the cross-bridge cycle, *Philos. Trans. R. Soc. London, Ser. B 359*, 1843−1855.
41. Mannherz, H. G., Schenck, H., and Goody, R. S. (1974) Synthesis of ATP from ADP and inorganic phosphate at the myosin-subfragment 1 active site, *Eur. J. Biochem. 48*, 287−295.
42. Goody, R. S., Hofmann, W., and Mannherz, H. G. (1977) The binding constant of ATP to myosin S1 fragment, *Eur. J. Biochem. 78*, 317−324.
43. Wakelin, S., Conibear, P. B., Woolley, R. J., Floyd, D. N., Bagshaw, C. R., Kovaács, M., and Málnási-Csizmadia, A. (2002) Engineering *Dictyostelium discoideum* myosin II for the introduction of site-specific fluorescence probes, *J. Muscle Res. Cell Motil. 23*, 673−683.

44. Trentham, D. R., Eccleston, J. F., and Bagshaw, C. R. (1976) Kinetic analysis of ATPase mechanisms, *Q. Rev. Biophys. 9*, 217−281.
45. Alberty, R. A. (2003) *Thermodynamics of biochemical reactions*, John Wiley and Sons, Hoboken, NJ.
46. Alberty, R. A. (2003) Thermodynamics of the hydrolysis of adenosine triphosphate as a function of temperature, pH, pMg, and ionic strength, *J. Phys. Chem. B 107*, 12324−12330.
47. Kull, F. J., Schlichting, I., Becker, A., Kollmar, M., Manstein, D. J., and Holmes, K. C. (2006) An alternate conformation for MgADP-beryllium fluoride bound myosin II (in press).
48. Brooks, B. R., Bruccoleri, R. E., Olafson, B. D., States, D. J., Swaminathan, S., and Karplus, M. (1983) CHARMM: A program for macromolecular energy, minimization and dynamics calculations, *J. Comput. Chem. 4*, 187−217.
49. Neria, E., Fischer, S., and Karplus, M. (1996) Simulation of activation free energies in molecular systems, *J. Chem. Phys. 105*, 1902−1921.
50. Eurenius, K. P., Chatfield, D. C., Brooks, B. R., and Hodoscek, M. (1996) Enzyme mechanisms with hybrid quantum and molecular mechanical potentials. I. Theoretical considerations, *Int. J. Quantum Chem. 60*, 1189−1200.
51. Schmidt, M. W., Baldridge, K. K., Boatz, J. A., Elbert, S. T., Gordon, M. S., Jensen, J. H., Koseki, S., Matsunaga, N., Nguyen, K. A., Su, S., Windus, T. L., Dupuis, M., and Montgomery, J. A., Jr. (1993) General atomic and molecular electronic structure system, *J. Comput. Chem. 14*, 1347−1363.
52. Schwarzl, S. M., Huang, D., Smith, J. C., and Fischer, S. (2005) Non-uniform charge scaling (NUCS): A practical approximation of solvent electrostatic screening in proteins, *J. Comput. Chem. 26*, 1359−1371.
53. Szabo, A., and Ostlund, N. S. (1996) *Modern Quantum Chemistry*, Dover, New York.
54. Binkley, J. S., Pople, J. A., and Hehre, W. J. (1980) Self-consistent molecular orbital methods. 21. Small split-valence basis sets for first-row elements, *J. Am. Chem. Soc. 102*, 939−947.
55. Gordon, M. S., Binkley, J. S., Pople, J. A., Pietro, W. J., and Hehre, W. J. (1982) Self-consistent molecular-orbital methods. 22. Small split-valence basis sets for second-row elements, *J. Am. Chem. Soc. 104*, 2797−2803.
56. Pietro, W. J., Francl, M. M., Hehre, W. J., DeFrees, D. J., Pople, J. A., and Binkley, J. S. (1982) Self-consistent molecular orbital methods. 24. Supplemented small split-valence basis sets for second-row elements, *J. Am. Chem. Soc. 104*, 5039−5048.
57. Hehre, W. J., Ditchfield, R., and Pople, J. A. (1972) Self-consistent molecular orbital methods. XII. Further extensions of Gaussian-type basis sets for use in molecular orbital studies of organic molecules, *J. Chem. Phys. 56*, 2257−2261.
58. Francl, M. M., Pietro, W. J., Hehre, W. J., Binkley, J. S., Gordon, M. S., DeFrees, D. J., and Pople, J. A. (1982) Self-consistent molecular orbital methods. XXIII. A polarization-type basis set for second-row elements, *J. Chem. Phys. 77*, 3654−3665.
59. Becke, A. D. (1993) Density-functional thermochemistry. III. the role of exact exchange, *J. Chem. Phys. 98*, 5648−5652.
60. Becke, A. D. (1988) Density-functional exchange-energy approximation with correct asymptotic behavior, *Phys. Rev. A 38*, 3098−3100.
61. Lee, C., Yang, W., and Parr, R. G. (1988) Development of the colle-salvetti correlation-energy formula into a functional of the electron density, *Phys. Rev. B 37*, 785−789.
62. Clark, T., Chandrasekhar, J., Spitznagel, G. W., and von Ragué Schleyer, P. (1983) Efficient diffuse function-augmented basis sets for anion calculations. III. the 3-21+G basis set for first-row elements, Li−F, *J. Comput. Chem. 4*, 294−301.
63. Zhao, Y., González-García, N., and Truhlar, D. G. (2005) Benchmark database of barrier heights for heavy atom transfer, nucleophilic substitution, association, and unimolecular reactions and its use to test theoretical methods, *J. Phys. Chem. A 109*, 2012−2018.
64. Rotzinger, F. P. (2005) Performance of molecular orbital methods and density functional theory in the computation of geometries of metal aqua ions, *J. Phys. Chem. B 109*, 1510−1527.
65. Curtiss, L. A., Raghavachari, K., Redfern, P. C., and Pople, J. A. (1997) Assessment of Gaussian-2 and density functional theories for the computation of enthalpies of formation, *J. Chem. Phys. 106*, 1063−1079.
66. Simons, J. (1982) Electron propagator studies of molecular anions, *Int. J. Quantum Chem. 16*, 575−581.
67. Skurski, P., Gutowski, M., and Simons, J. (2000) How to choose a one-electron basis set to reliably describe a dipole-bound anion, *Int. J. Quantum Chem. 80*, 1024−1038.
68. Raghavachari, K., and Anderson, J. B. (1996) Electron correlation effects in molecules, *J. Phys. Chem. 100*, 12960.
69. Fischer, S., and Karplus, M. (1992) Conjugate peak refinement: An algorithm for finding reaction paths and accurate transition states in systems with many degrees of freedom, *Chem. Phys. Lett. 194*, 252−261.
70. Fischer, S., Michnick, S., and Karplus, M. (1993) A mechanism for rotamase catalysis by the FK506 binding protein (FKBP), *Biochemistry 32*, 13830−13837.
71. Bondar, A. N., Elstner, M., Suhai, S., Smith, J. C., and Fischer, S. (2004) Mechanism of primary proton tranfer in bacteriorhodopsin, *Structure 12*, 1281−1288.
72. Gruia, A., Bondar, A. N., Smith, J. C., and Fischer, S. (2005) Mechanism of a molecular valve in the halorhodopsin chloride pump, *Structure 13*, 617−627.
73. Bash, P. A., Field, M. J., Davenport, R. C., Petsko, G. A., Ringe, D., and Karplus, M. (1991) Computer simulation and analysis of the reaction pathway of triosephosphate isomerase, *Biochemistry 30*, 5826−5832.
74. Mulliken, R. S. (1955) Electronic population analysis on LCAO-MO molecular wave functions. I, *J. Chem. Phys. 23*, 1833−1840.
75. Akola, J., and Jones, R. O. (2003) ATP hydrolysis in water: A density functional study, *J. Phys. Chem. B 107*, 11774−11783.
76. Tuckerman, M. E., Marx, D., and Parrinello, M. (2002) The nature and transport mechanism of hydrated hydroxide ions in aqueous solution, *Nature 417*, 925−929.
77. Wang, Y.-N., Topol, I. A., Collins, J. R., and Burt, S. (2003) Theoretical studies on the hydrolysis of mono-phosphate and triphosphate in gas phase and aqueous solution, *J. Am. Chem. Soc. 125*, 13265−13273.
78. Furch, M., Fujita-Becker, S., Geeves, M. A., Holmes, K. C., and Manstein, D. J. (1999) Role of the salt-bridge between switch-1 and switch-2 of *Dictyostelium* myosin, *J. Mol. Biol. 290*, 797−809.
79. Florián, J., Åqvist, J., and Warshel, A. (1998) On the reactivity of phosphate monoester dianions in aqueous solution: Bronsted linear free-energy relationships do not have an unique mechanistic interpretation, *J. Am. Chem. Soc. 120*, 11524−11525.
80. Mercero, J. M., Barrett, P., Lam, C. W., Fowler, J. E., Ugalde, J. M., and Pedersen, L. G. (2000) Quantum mechanical calculations on phosphate hydrolysis reactions, *J. Comput. Chem. 21*, 43−51.
81. Hu, C.-H., and Brinck, T. (1999) Theoretical studies of the hydrolysis of the methyl phosphate anion, *J. Phys. Chem. A 103*, 5379−5386.
82. Florián, J., and Warshel, A. (1997) A fundamental assumption about $OH^-$ attack in phosphate ester hydrolysis is not fully justified, *J. Am. Chem. Soc. 119*, 5473−5474.
83. Florián, J., and Warshel, A. (1998) Phosphate ester hydrolysis in aqueous solution: Associative versus dissociative mechanisms, *J. Phys. Chem. B 102*, 719−734.
84. Åqvist, J., Kolmodin, K., Florián, J., and Warshel, A. (1999) Mechanistic alternatives in phosphate monoester hydrolysis: What conclusions can be drawn from available experimental data? *Chem. Biol. 6*, R71−R80.
85. Sasaki, N., Shimada, T., and Sutoh, K. (1998) Mutational analysis of the switch II loop of *Dictyostelium* myosin II, *J. Biol. Chem. 273*, 20334−20340.
86. Friedman, A. L., Geeves, M. A., Manstein, D. J., and Spudich, J. A. (1998) Kinetic characterization of myosin head fragment with long-lived myosin·ATP states, *Biochemistry 37*, 9679−9687.
87. Saint-Martin, H., Ruiz-Vicent, L. E., Ramírez-Solís, A., and Ortega-Blake, I. (1996) Toward an understanding of the hydrolysis of Mg−$PP_i$. An *ab initio* study of the isomerization reactions of neutral and anionic Mg-pyrophosphate complexes, *J. Am. Chem. Soc. 118*, 12167−12173.
88. Hammond, G. S. (1955) A correlation of reaction rates, *J. Am. Chem. Soc. 77*, 334−338.
89. Alberty, R. A., and Goldberg, R. N. (1992) Standard thermodynamic formation properties for the adenosine 5′-triphosphate series, *Biochemistry 31*, 10610−10615.
90. Holmes, K. C., Angert, I., Kull, F. J., Jahn, W., and Schröder, R. R. (2003) Electron cryo-microscopy shows how strong binding of myosin to actin releases nucleotide, *Nature 425*, 423−427.

91. Coureux, P.-D., Wells, A. L., Ménétrey, J., Yengo, C. M., Morris, C. A., Sweeney, H. L., and Houdusse, A. (2003) A structural state of the myosin V motor without bound nucleotide, *Nature 425*, 419−423.
92. Conibear, P. B., Bagshaw, C., Fajer, P. G., Kovács, M., and Málnási-Csizmadia, A. (2003) Myosin cleft movement and its coupling to actomyosin dissociation, *Nat. Struct. Biol. 10*, 831−835.
93. Goody, R. S. (2003) The missing link in the muscle cross-bridge cycle, *Nat. Struct. Biol. 10*, 773−775.
94. Coureux, P.-D., Sweeney, H. L., and Houdusse, A. (2004) Three myosin V structures delineate essential features of chemo-mechanical transduction, *EMBO J. 23*, 4527−4537.
95. Reubold, T., Eschenburg, S., Becker, A., Kull, F. J., and Manstein, D. J. (2003) A structural model for actin-induced nucleotide release in myosin, *Nat. Struct. Biol. 10*, 826−830.
96. Lawson, J. D., Pate, E., Rayment, I., and Yount, R. G. (2004) Molecular dynamics analysis of structural factors influencing back door $P_i$ release in myosin, *Biophys. J. 86*, 3794−3803.
97. Dudev, M., Wang, J., Dudev, T., and Lim, C. (2006) Factors governing the metal coordination number in metal complexes from cambridge structural database analyses, *J. Phys. Chem. B 110*, 1889−1895.
98. Yount, R. G., and Koshland, D. E., Jr. (1963) Properties of the $O^{18}$ exchange reaction catalyzed by heavy meromyosin, *J. Biol. Chem. 238*, 1708−1713.
99. Webb, M. A., Ash, D. E., Leyh, T. S., Trentham, D. R., and Reed, G. H. (1982) Electron paramagnetic resonance studies of Mn(II) complexes with myosin subfragment 1 and oxygen 17-labeled ligands, *J. Biol. Chem. 257*, 3068−3072.
100. Topol, I. A., Cachau, R. E., Nemukhin, A. V., Grigorenko, B. L., and Burt, S. K. (2004) Quantum chemical modeling of the GTP hydrolysis by the RAS-GAP protein complex, *Biochim. Biophys. Acta 1700*, 125−136.
101. Dittrich, M., Hayashi, S., and Schulten, K. (2003) On the mechanism of ATP hydrolysis in $F_1$-ATPase, *Biophys. J. 85*, 2253−2266.
102. Dittrich, M., Hayashi, S., and Schulten, K. (2004) ATP hydrolysis in the $\beta_{TP}$ and $\beta_{DP}$ catalytic sites of $F_1$ATPase, *Biophys. J. 87*, 2954−2967.
103. Voityuk, A. A., and Rösch, N. (2000) AM1/d parameters for molybdenum, *J. Phys. Chem. A 104*, 4089−4094.
104. Lopez, X., and York, D. M. (2003) Parametrization of semiempirical methods to treat nucleophilic attacks to biological phosphates: AM1/d parameters for phosphorus, *Theor. Chem. Acc. 109*, 149−159.
105. Winget, P., Horn, A. H. C., Selcuki1, C., Martin, B., and Clark, T. (2003) AM1* parameters for phosphorus, sulfur and chlorine, *J. Mol. Model. 9*, 408−414.
106. Thiel, W., and Voityuk, A. A. (1996) Extension of MNDO to d orbitals: Parameters and results for the second-row elements and for the zinc group, *J. Phys. Chem. 100*, 616−626.
107. Gregersen, B. A., Lopez, X., and York, D. M. (2003) Hybrid QM/MM study of thio effects in transphosphorylation reactions, *J. Am. Chem. Soc. 125*, 7178−7179.
108. Cui, Q., Elstner, M., Kaxiras, E., Frauenheim, T., and Karplus, M. (2001) A QM/MM implementation of the self-consistent charge density functional tight binding (SCC-DFTB) method, *J. Phys. Chem. B 105*, 569−585.
109. Pai, E. F., Krengel, U., Petsko, G. A., Goody, R. S., Kabsch, W., and Wittinghofer, A. (1990) Refined crystal structure of the triphosphate conformation of H-*ras* p21 at 1.35 Å resolution: Implications for the mechanism of GTP hydrolysis, *EMBO J. 9*, 2351−2359.
110. Scheffzek, K., Ahmadian, M. R., Kabsch, W., Wiesmüller, L., Lautwein, A., Schmitz, F., and Wittinghofer, A. (1997) The Ras-RasGAP complex: Structural basis for GTPase activation and its loss in oncogenic Ras mutants, *Science 277*, 333−338.

BI052433Q